UNIVERSITY OF OKLAHOMA

GRADUATE COLLEGE

# LASER COOLING AND TRAPPING USING LAGUERRE-GAUSSIAN LASER BEAMS

A Dissertation

SUBMITTED TO THE GRADUATE FACULTY

in partial fulfillment of the requirements for the

degree of

Doctor of Philosophy

By

Sharon A. Kennedy

Norman, Oklahoma

2003

Downloaded from SHAREOK. Persistent Handle URL: https://hdl.handle.net/11244/651

UMI Number: 3107291

INFORMATION TO USERS

The quality of this reproduction is dependent upon the quality of the copy submitted. Broken or indistinct print, colored or poor quality illustrations and photographs, print bleed-through, substandard margins, and improper alignment can adversely affect reproduction.

In the unlikely event that the author did not send a complete manuscript and there are missing pages, these will be noted. Also, if unauthorized copyright material had to be removed, a note will indicate the deletion.

UMI®

UMI Microform 3107291

Copyright 2004 by ProQuest Information and Learning Company.

All rights reserved. This microform edition is protected against unauthorized copying under Title 17, United States Code.

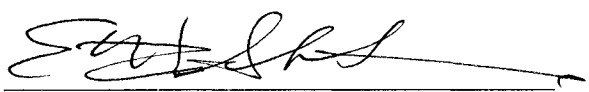
ProQuest Information and Learning Company
300 North Zeeb Road
P.O. Box 1346
Ann Arbor, MI 48106-1346

© Copyright by Sharon A. Kennedy 2003
All Rights Reserved.

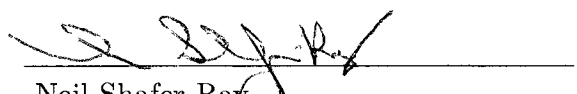
LASER COOLING AND TRAPPING USING LAGUERRE-GAUSSIAN LASER BEAMS

A Dissertation APPROVED FOR THE
DEPARTMENT OF PHYSICS AND ASTRONOMY

**By**



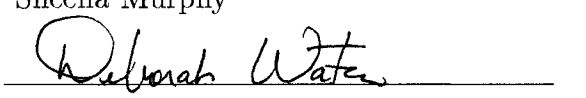
Eric R. I. Abraham



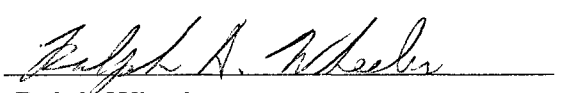
Neil Shafer-Ray



Sheena Murphy



Deborah Watson



Ralph Wheeler

# Acknowledgements

I would like to thank Digital Optics Corporation and the University of Oklahoma for their funding of my work. I would like to thank the undergraduates, most especially Matt Szabo, Grant Biedermann, and Tom Farrar, who have worked in the lab and whose help was very appreciated.

Most especially, I appreciate my family. Many times it was their encouragement that kept me going. They have been patient through the long nights, and have been there for me through all of my disappointments. Josh has been the most patient and understanding child. Bil has been my backbone when I needed one. He pushed me when I needed it, held my hand, and provided a shoulder to cry on.

# Contents

**Acknowledgements** iv

**Abstract** vii

**1 Introduction** 1

**2 Laser Cooling and Trapping** 4
- 2.1 Introduction . . . 4
- 2.2 Laser Cooling . . . 5
- 2.3 Magneto-Optical Trap . . . 6
- 2.4 MOT construction . . . 8
- 2.5 Determining the MOT Characteristics . . . 12

**3 Laguerre-Gaussian laser beams** 16
- 3.1 Introduction . . . 16
- 3.2 Description of Laguerre-Gaussian laser beams . . . 17
- 3.3 Creation of Laguerre-Gaussian laser modes . . . 18
- 3.4 Laguerre-Gaussian beam analysis . . . 22
- 3.5 Conclusion . . . 29

**4 Confinement of Atoms in a Laguerre-Gaussian Laser Beam** 31
- 4.1 Introduction . . . 31
- 4.2 Experimental Setup . . . 32
- 4.3 Confinement of atoms in a blue-detuned $LG_0^1$ laser beam . . . 33
- 4.4 Confinement of atoms in a red-detuned $LG_0^1$ laser beam . . . 36
- 4.5 Conclusion . . . 39

**5 Properties of Bose-Einstein condensates in external potentials** 41
- 5.1 Introduction . . . 41
- 5.2 Three Dimensional Simple Harmonic Oscillator . . . 46
- 5.3 Toroid . . . 48
- 5.4 Experimentally realistic toroid . . . 49

**6 Conclusion** 52

**Appendix A**
Diode Lasers . . . . . 54
A.1 Introduction . . . . . 54
A.2 Construction of a diode laser . . . . . 55
A.2.1 Description of parts . . . . . 55
A.2.2 Construction of the diode assembly . . . . . 58
A.2.3 Diode mounting and collimation . . . . . 60
A.2.4 Grating alignment . . . . . 62
A.3 Temperature Control . . . . . 65
A.4 Tuning the laser . . . . . 66
A.5 Master Oscillator Power Amplifier . . . . . 68

**Appendix B**
Locking the Laser to Atomic Transitions . . . . . 71
B.1 Introduction . . . . . 71
B.2 Saturated Absorption Spectroscopy . . . . . 72
B.3 Dichroic Atomic Vapor Laser Lock (DAVLL) . . . . . 74
B.4 Sidelock Servo Box . . . . . 75

**Appendix C**
Vacuum . . . . . 80
C.1 Vacuum pumps . . . . . 80
C.2 Cleaning . . . . . 82
C.3 Assembly . . . . . 83
C.4 Pumping Down . . . . . 84
C.5 Baking . . . . . 85

**Bibliography** **86**

# Abstract

Laser cooling and trapping has led to a revolution in Atomic and Molecular physics. Optical traps created with blue-detuned laser beams are desired for numerous studies. One method of creating such a trap is with Laguerree-Gaussian laser beams.

Laguerre-Gaussian ($LG$) laser beams are interesting because of their orbital angular momentum and radial intensity nodes. Previous methods of creating higher-order $LG$ beams did not yield pure $LG$ modes. In collaboration with Digital Optics Corporation diffraction optics have been manufactured that yield higher-order $LG$ laser beams with purities consistent with 100% of the intensity in the desire mode. We then create a donut-mode $LG$ beam with this method to confine atoms from a MOT in both a blue-detuned and a red-detuned optical dipole force trap.

# Chapter 1

# Introduction

In 1997 the Nobel Prize was awarded to Steven Chu [1], William Phillips [2], and Claude Cohen-Tannoudji [3] for their work in laser cooling and trapping. Laser cooling and trapping has led to many advances in atomic physics, including Bose-Einstein condensation (BEC) for which Eric Cornell, Carl Wieman [4], and Wolfgang Ketterle [5] won the Nobel Prize in 2001.

Atoms can be trapped in optical dipole traps, which require no magnetic fields. If the trap is constructed from red-detuned laser beams, then the atoms will be confined within the high-intensity regions of the laser field. Blue-detuned lasers repel atoms from the high intensity regions. Most optical dipole traps are created using a focused red-detuned Gaussian laser beam [6, 7]. Blue-detuned optical dipole traps offer the advantages that the atoms are confined in a nearly interaction-free region of space [8], however these traps are more difficult to experimentally realize.

One possible geometry of such a trap uses Laguerre-Gaussian ($LG$) laser beams, which possess radial nodes and a stable central node due to their quantized orbital angular momentum [9]. The most common method of obtaining $LG$ laser beams

external to the laser cavity is with computer generated holograms. These holograms work very well for doughnut mode beams (beams with only a central intensity node); however these holograms are unable to yield pure higher-order modes (modes with additional radial intensity nodes) [10]. We are able to create higher-order *LG* beams with a mode purity consistent with 100% of the laser intensity in the desired mode using diffractive optics [11].

Applications of ultra-cold atoms trapped in blue-detuned optical dipole traps include more precise atomic clocks [12], which are limited by the interaction time [13]. Atomic fountains have increased the interaction time over traditional atomic beams to about one second [14], but adds uncertainty due to collisions between the atoms [15, 16]. By using ultra-cold atoms confined to the dark regions of a blue-detuned trap using *LG* laser beams, the interaction time can be increased to hundreds of seconds. Additional motivation for the trapping of ultra-cold atoms in a blue-detuned trap created with higher-order *LG* beams is that vortices in a Bose-Einstein condensate trapped in concentric rings of a higher-order *LG* beam may be observed using matter-wave interference [17]. Also, these condensates may be useful as a rotational gyroscopes [18].

With these motivations, we have created very pure higher-order *LG* beams from the Gaussian output of a diode laser using diffractive optics. Chapter A details the construction of the external cavity diode lasers used in our lab. Laguerre-Gaussian laser beams, the method we use to create these beams, and detailed analysis of our beams are presented in Chapter 3. I present the analysis of ultra-cold $^{87}$Rb atoms confined to the node of a blue-detuned doughnut mode beam and to the anti-node of

a red-detuned doughnut mode beam in Chapter 4. Chapter 2 describes the magneto-optical trap from which we load the atoms into the optical trap created with the *LG* beam. The vacuum system is discussed in Chapter C, and the methods by which we lock our lasers to the desired frequencies are discussed in Chapter B. Finally, in Chapter 5 some theoretical calculations for a BEC created in a toroidal trap formed with *LG* beams are presented.

# Chapter 2

# Laser Cooling and Trapping

## 2.1 Introduction

The 1997 Nobel Prize in physics was awarded to Steven Chu [1], William Phillips [2], and Claude Cohen-Tannoudji [3] for their work in laser cooling. The cooling and trapping of neutral atoms has led to many new advances in atomic, molecular, and optical physics. The most notable achievement arising from laser cooling is Bose-Einstein condensation (BEC) of dilute gases. BEC was first observed in 1995 by Eric Cornell and Carl Wieman in a gas of Rubidium atoms [19]. Shortly after Eric Cornell and Carl Wieman reported the first BEC, Randall Hulet reported a BEC in a gas of Lithium atoms [20]. Wolfgang Ketterle followed quickly with a BEC in a gas of Sodium atoms [21]. Eric Cornell, Carl Wieman, and Wolfgang Ketterle were awarded the Nobel Prize in physics for their work in BEC in 2001 [4, 5].

The most robust trap for the study of ultra-cold atoms is the magneto-optical trap (MOT). For application such as BEC, atoms are transferred from the MOT into a magnetic trap. Atoms can also be transferred from the MOT into an optical

dipole force trap. In this chapter I describe laser cooling and the construction of our most recent MOT. This MOT is formed in a unique rectangular glass vacuum cell that offers increased optical access over other cells commonly used. This optical access is important to the geometry of our experiments with confining ultra-cold atoms in Laguerre-Gaussian beams described in Chapter 4.

## 2.2 Laser Cooling

Laser cooling uses the momentum of photons to slow and cool atoms. This is now a commonly used method of obtaining ultra-cold atoms. A good reference is *Laser Cooling and Trapping* by Harold Metcalf and Peter van der Straten [22].

If a photon with momentum $\hbar\vec{k}$ is in resonance with an atomic transition, then it may be absorbed by an atom. Atoms are not stationary, however, so the frequency of the photon in the atom's frame of motion is Doppler shifted by an amount $\nu_D = -\vec{k} \cdot \vec{v}$, where $\vec{v}$ is the velocity of the atom. If the atom is traveling in a laser field tuned to the red of the resonance frequency, the atom will absorb photons opposing its direction of travel.

After a photon is absorbed, the atom is pumped into an excited state. It has also experienced a change in momentum of $\hbar\vec{k}$. After an average time $\tau$, the excited state lifetime, the atom will re-emit the photon either by stimulated or spontaneous emission. When the photon is emitted via stimulated emission, the photon is emitted in the direction of the laser field and the atom experiences a change in momentum of $-\hbar\vec{k}$. The system then returns to its original state. When the photon is emitted

by spontaneous emission the direction in which it is emitted is random, and the atom's momentum changes by $\hbar\vec{k}'$. After many photons are re-emitted, the average change in momentum of the atom due to spontaneous emission is 0 as the photon is always emitted in a random direction. The absorption and spontaneous emission of photons can then be used to slow and cool the atoms.

An optical molasses can be formed by directing three red-detuned laser beams in orthogonal directions and reflecting the beams so that the reflected beams overlap the incoming beams. In the region where the beams intersect, there are always photons opposing the motion of the atoms regardless of the direction of the atoms. The force felt by the atoms, however, is velocity dependent only and the atoms are not trapped within this region, but only slowed. A position dependent restoring force is also needed in order for the atoms to be spatially trapped.

## 2.3 Magneto-Optical Trap

A simple and convenient way in which $\sim 10^8$ atoms with a temperature $< 1$ mK can be collected is with a magneto-optical trap (MOT). The atoms are cooled via Doppler cooling from three sets of orthogonal and retro-reflected laser beams as described above. A spatially dependent restoring force is obtained from a linearly varying magnetic field. An understanding of the mechanisms by which a MOT works is best obtained by examining a two-level atom in one dimension.

The atomic levels of an atom within a magnetic field varying linearly in space ($B \propto z$) are split as shown in Figure 2.1. The atoms are also in a laser field

made of 2 circularly polarized and opposing laser beams with frequency, $\omega_l$. These lasers are detuned to the red of the non-Zeeman shifted atomic transition frequency. Right circularly polarized light ($\sigma_+$) incident from the left will excite atoms from the $m_g = 0$ state to the $m_e = 1$ state ($\Delta m = +1$). Similarly, left circularly polarized light ($\sigma_-$) will excite atoms from the $m_g = 0$ state to the $m_e = -1$ state ($\Delta m = -1$).

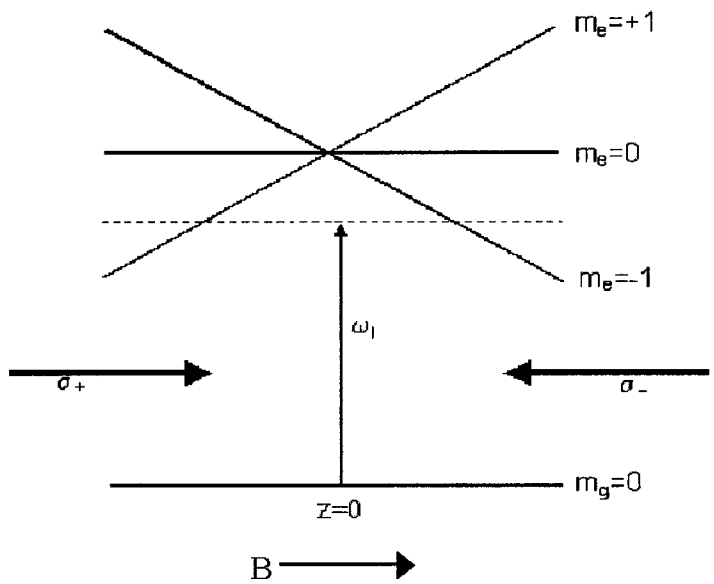



Figure 2.1: This figure shows the Zeeman splitting of the atomic sublevels in a magnetic field of the form $B(z) \propto z$. If an atom is located at $z > 0$, then it will feel $\sigma_-$ light pushing it towards the center. If an atom is located at $z < 0$ then it will feel $\sigma_+$ light pushing it towards the center.

If an atom is located at $z > 0$, then the laser will be near the $m_g = 0 \rightarrow m_e = -1$ transition. The atom will feel $\sigma_-$ light pushing it back towards the center. Likewise, an atom located at $z < 0$ will feel $\sigma_+$ light pushing it towards the center. Thus, the atom experiences a position dependent restoring force pushing it towards the center as required to have a trap.

## 2.4 MOT construction

Our MOT is formed from Rb vapor in a rectangular glass cell. The sides of the cell are optically flat for the laser beams to pass through. A small glass ampule of Rb metal is placed inside a tube connected to the vacuum chamber below the glass cell. After the system is pumped down, we break the ampule by squeezing the tube with a pair of pliers. When the ampule is first broken, a pressure spike is generally observed as the air inside the ampule is released. Breaking the ampule exposes the Rb to the vacuum, and the vapor is generated from the outgassing metal. The vapor pressure can be adjusted by heating or cooling the tube containing the Rb. The experimental setup of our MOT is shown in Figure 2.2.

The construction of the MOT begins with construction of laser diodes as described in Chapter A. The MOT requires two lasers: one in a master oscillator-power amplifier (MOPA) configuration tuned to the $^2S_{1/2},\ F = 2 \rightarrow\ ^2P_{3/2},\ F' = 3$ cycling transition at 384228 GHz, the other laser is tuned to the $^2S_{1/2},\ F = 1 \rightarrow\ ^2P_{3/2},\ F' = 2$ repump transition at 384234 GHz [23]. A saturated absorption spectrometer (Section B.2) is used with the repump to show where the atomic transitions are. The cycling laser and the repump laser are both locked using a DAVLL as described in Section B.3.

The magnetic coils are constructed by winding magnet wire so that there are two rings with the appropriate diameter and number of turns. For the true anti-Helmholtz configuration, the distance between the coils should be equivalent to their radius. The coils should also be designed such that the magnetic field is about

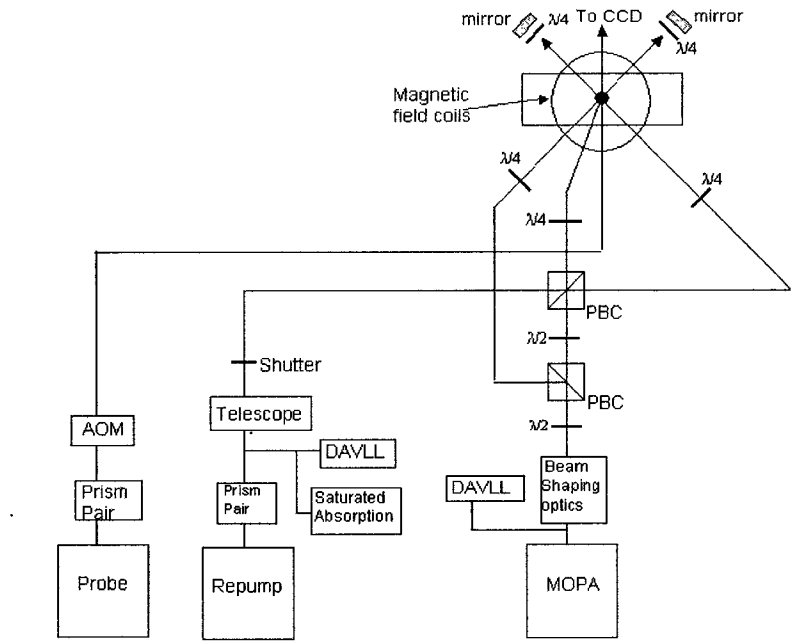



Figure 2.2: This is a schematic of the experimental setup for our MOT. The laser driving the cycling transition is provided by the MOPA. Using polarizing beam splitter cubes (PBCs) the laser beam is split into three separate beams. We use a rectangular glass cell and direct two of the laser beams at 45° with respect to the cell. The third laser beam is directed along the magnetic field axis horizontal to the table. The repump is brought in through the back of one of the PBCs. The probe is directed vertically up and used for absorption imaging as described in Section 2.5.

10 G/cm. The coils are mounted in the anti-Helmholtz configuration with care taken that the projected beam path is not blocked in any way.

The output of the MOPA is shaped using cylindrical lenses, sent through an optical isolator, and then telescoped to a $1/e^2$ radius of 12.5 mm. The laser beam is sent through a $\lambda/2$ plate to change its polarization. It is then sent through a polarizing beam splitter cube, which separates the two orthogonal components. There are now two beams, one of which is sent through another $\lambda/2$ plate and another polarizing beam splitter cube. The $\lambda/2$ plates are adjusted so that there is equal intensity in each of the three beams.

The three beams are then each directed through a $\lambda/4$ plate that will transform the linear polarized light to circularly polarized. The beam traveling in the direction of the magnetic field should be polarized in the opposite direction of the remaining two beams. When aligning the $\lambda/4$ plate, it should be rotated such that its fast access is at $\pm 45°$ from the polarization of the linearly polarized beam to obtain right or left ($\sigma_+$ or $\sigma_-$) circularly polarized light. We determine that the $\lambda/4$ plate is rotated properly by directing the circularly polarized beam through a linear polarizer and into a power meter. Circularly polarized light is composed of equal components of horizontal and vertical linearly polarized light. If the beam is circularly polarized, then the power measured with the power meter will not change as the linear polarizer is rotated. If, however, the beam is more elliptically polarized, then the power measured will resemble a Sine curve as the polarizer is rotated.

The three circularly polarized beams are then directed in orthogonal directions through the vapor cell. When they exit the cell they pass through another $\lambda/4$ plate and then are retro-reflected. For proper alignment of the retro-reflected beams, we use an iris before the first polarizing beam splitter cube to decrease the size of the beam. We then insure that the retro-reflected beam overlaps the original beam.

The repump beam is also telescoped to a $1/e^2$ radius of 12.5 mm. It is then directed through the back of one of the polarizing beam splitter cubes so that it overlaps the three MOT beams. For proper alignment, we decrease the power in the MOT beams by decreasing the current in the MOPA, as these beams are generally so much brighter than the repump beam. We then place an iris in the repump and one in the MOT beam before the first polarizing beam splitter cube and overlap the

repump with one of the MOT beams, following the beam path until the beams enter the cell.

We use security cameras to observe our MOT. The camera is placed so that the intersection of the beams is in its field of view and the lens is adjusted so that it is focused near the center of the glass chamber. While observing the repump laser's saturated absorption signal on the oscilloscope, the Ramp Gain is turned down and the PZT bias is adjusted until the saturated absorption peaks take the entire display and the laser is ramping over the peaks only. Once the DAVLL curves have been verified for the cycling laser, the Ramp is turned off and the PZT Bias is slowly adjusted over its range while observing the security camera monitor. At some point in the tuning range, a small white flashing ball should be observed on the monitor. This is the MOT forming and dissipating as the repump ramps over the $^{87}\mathrm{Rb}\ ^2S_{1/2}, F = 1 \rightarrow^2 P_{3/2}, F' = 2$ transition. The cycling laser can then be locked. While observing the monitor, the repump's ramp is further turned down, and the Bias is adjusted for the maximum number of atoms in the MOT.

If the flashing ball is not observed over the cycling laser's adjustment range there are several things to check for. The magnetic coils may be in the Helmholtz configuration, rather than the anti-Helmholtz configuration, or, more likely, there is a problem with the polarization. The current direction is reversed first. If the MOT is still not observed, then the polarizations of the three beams are switched individually until the MOT is seen. If the MOT is still not observed, then the lasers should be confirmed to be single mode and lasing at the appropriate frequency. It

may also be easier to see if the Rb metal is heated slightly so that there is a greater vapor pressure.

## 2.5 Determining the MOT Characteristics

Once a MOT has been constructed, the MOT characteristics can give valuable information. These characteristics include the number of atoms confined and the temperature. Two methods are used in our lab to determine the number of atoms in the MOT. One is to measure the MOT fluorescence on a calibrated photodiode. The other is to measure the absorption of a probe laser on resonance with the atomic transition.

A photodiode offers a quick method of determining the number of atoms. Using a lens the fluorescence is focused onto the photodiode. The output of the photodiode is converted to the light power using the calibration curve as shown in Figure 2.3. Only a fraction of the fluorescence from the MOT reaches the photodiode. This fraction is determined as $\Omega = \frac{\pi r^2}{4\pi R^2}$, where $r$ is the radius of the lens, and $R$ is the distance from the center of the MOT to the lens. The total fluorescence emitted from the MOT is $\frac{Nh\nu}{2\tau}$, where $N$ is the number of atoms in the MOT, $h\nu$ is the energy of a photon at the $^2S_{1/2}, F = 2 \rightarrow ^2 P_{3/2}, F' = 3$ $^{87}$Rb transition and $\tau$ is the lifetime of the excited state, which is 27 ns for $^{87}$Rb [23]. The fluorescence measured by the photodiode is then

$$\frac{Nh\nu\Omega}{2\tau} = P, \tag{2.1}$$

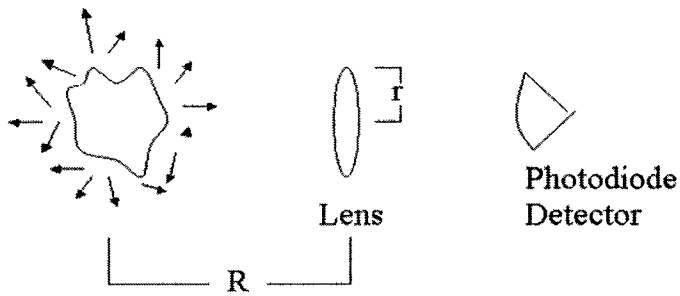



Figure 2.3: This figure shows the configuration required to use a photodiode to measure the fluorescence and determine the number of atoms in the MOT.

where P is the power measured by the photodiode. This relation can then be used to approximate the number of atoms in the MOT.

Another method for more accurately determining the number of atoms in the MOT is by measuring the absorption of a weak probe laser on resonance with the $^2S_{1/2}, F = 2 \rightarrow^2 P_{3/2}, F' = 3$ transition. The absorption profile can be observed by directing the probe onto a CCD camera. When the probe is aligned and on resonance, a shadow of the MOT can be seen when viewing the CCD image on a monitor.

To determine the number of atoms in the MOT, we optically pump the atoms into the $^2S_{1/2}, F = 2$ state using the repump beam with the MOT beams turned off. We flash the probe and obtain an image after it has passed through the MOT using a frame-grabber coordinated through LabVIEW. We let the atoms in the MOT dissipate and repeat the image acquisition sequence. This second image does not pass through the MOT and is used for normalization. We normalize the absorption

image by the second image. The resultant image has values between 0 and 1 at each pixel, where areas with no atoms have a value of 1. The lower the value, the higher the column density, $n(x, y)$: the number of atoms located in a rectangular column with a cross-section equivalent to the area of a pixel ($n(x, y) = \frac{N(x,y)}{A}$, where $A$ is the area of a pixel). A typical absorption image of a MOT is shown in Figure 2.4.

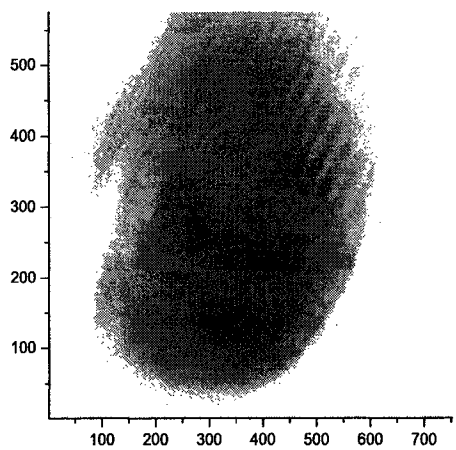



Figure 2.4: This figure shows a typical absorption image of a MOT. The darker the area, the larger the number of atoms. In areas that the probe did not pass through any atoms, the image has a value of 1.0 and corresponds to the color white.

The normalized absorption image then has the mathematical form:

$$f(x, y) = e^{-n(x,y)\sigma}, \tag{2.2}$$

where $\sigma$ is the scattering cross section. The number of atoms in each column is determined by multiplying the area of each CCD pixel by the column density. If the probe is larger than the MOT, then the total number of atoms in the MOT is determined by summing up the number of atoms in each column.

With absorption imaging, the temperature of the MOT is also easily obtained. When the MOT beams are turned off, the confining potential is eliminated. The distribution of atoms in the MOT then begins to expand according to its temperature. An image is taken as described above with the probe flashed at some time $t$ after the MOT beams are turned off. The MOT is reformed, and the image acquisition is repeated. This time, the probe is flashed at some other time $t'$ after the MOT beams are turned off. The full-width half-max of the Gaussian profiles of the two images is obtained and the velocity is determined from the difference of the two full-width half-maxima divided by $t' - t$. The temperature of the atoms in the MOT is then easily derived:

$$\frac{1}{2}Mv^2 = \frac{3}{2}k_B T. \tag{2.3}$$

We typically have MOTs with more than $10^8$ atoms at temperatures less than 1 mK.

# Chapter 3

# Laguerre-Gaussian laser beams

## 3.1 Introduction

Laser cooling and trapping yields collections of cold atoms, typically with temperatures less than 0.1 mK. These cold atoms have proven to be useful in precision experiments, as Doppler broadening has been minimized due to their low velocities; however, the atoms are generally confined to regions of high laser intensity, which induces an AC Stark shift that shifts the energy difference between the atomic levels. Therefore, optical traps in which the laser fields interact minimally with the atoms may be useful for precision experiments, such as atomic clocks. Such traps may be realized utilizing blue-detuned Laguerre-Gaussian ($LG$) laser beams. Multiple Bose-Einstein condensates (BEC's) may be confined in the concentric rings of laser traps created from higher-order $LG$ laser beams. Vortices in these multiple BEC's may be observed using matter wave interference [17].

## 3.2 Description of Laguerre-Gaussian laser beams

Laguerre-Gaussian laser beams ($LG_p^\ell$) have a radial electric field proportional to a Gaussian multiplied by an associated Laguerre polynomial, $L_p^\ell$ [9].

$$u_p^\ell(r,\phi) = \sqrt{\frac{2P}{\pi w^2}}\sqrt{\frac{p!}{(\ell+p)!}}(-1)^p e^{-\imath\ell\phi} e^{-r^2/w^2}\left(\frac{\sqrt{2}r}{w}\right)^\ell L_p^\ell\left(\frac{2r^2}{w^2}\right), \tag{3.1}$$

where $P$ is the laser power and $w$ is the beam waist. The intensity of the $LG$ beam is $u^*u$. These laser modes then consist of $p+1$ radial nodes and an azimuthal phase change of $2\pi\ell$ in the electric field given by the $e^{-\imath\ell\phi}$ term in the above equation. The azimuthal phase change results in a phase singularity in the electric field and a stable intensity node at the center of the beam. These beams also possess a quantized angular momentum of $\ell\hbar$ per photon. A Gaussian beam occurs when $\ell = p = 0$, whereas a donut mode is an $LG$ mode with $p = 0$ and $\ell > 0$. As $\ell$ increases, so does the size of the central node. Theoretical beam profiles of $LG_p^\ell$ modes that we are able to create are shown in Fig. 3.1. In this figure, (a) is a theoretical intensity profile of an $LG_0^1$ mode, and (b) is that of an $LG_0^5$ mode. The intensity node of the $LG_0^5$ mode is larger than that of the $LG_0^1$ mode and the intensity peak is not as large. Figures 3.1 (c) and (d) show an $LG_1^2$ mode and an $LG_1^{10}$ mode. Here we see that there are two nodes: the central node and one annular node. The central node of the $LG_1^{10}$ node is larger than that of the $LG_1^2$ node as expected. Figure 3.1 (e) shows an $LG_2^3$ laser mode which has the one central node and two annular nodes.

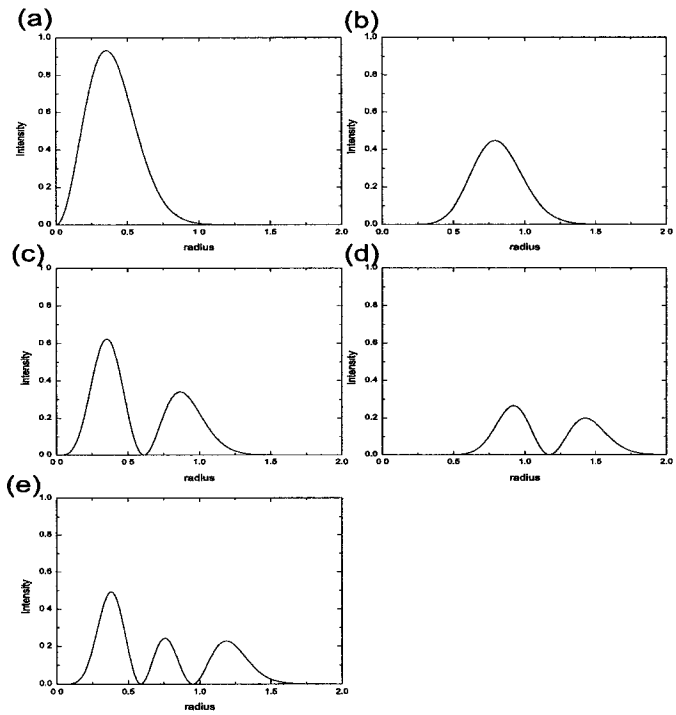



Figure 3.1: Shown here are theoretical cross-sections of Laguerre-Gaussian beams that we can create using our optics. (a) The "doughnut mode" $LG_0^1$ laser mode. (b) $LG_0^5$ laser mode. This beam is also a doughnut mode, but the size of the central node has increased compared with the $LG_0^1$ mode shown in (a). (c) The $LG_1^2$ mode. Here, we see that the beam has the central node and 1 additional annular node. (d) The $LG_1^{10}$ mode. This mode also has two nodes like in (b), but a larger central node due to the increase in $\ell$. (e) An $LG_2^3$ mode. This mode has the central node and 2 additional annular nodes.

## 3.3 Creation of Laguerre-Gaussian laser modes

Laguerre-Gaussian laser modes can be created inside the laser cavity [24] or converted from a Hermite-Gaussian laser mode [25, 26]; however, because we use diode lasers in our experiments, an external cavity method of converting from a Gaussian mode to an $LG$ mode is necessary. Previously used methods of external conversion from a Gaussian mode to an $LG$ mode include spiral phase plates, computer generated holograms, and diffractive optics.

Spiral phase plates are used to convert Gaussian beams to $LG$ beams, and can also be used to convert between two $LG_p^\ell$ beams [27, 28]. These are transmission optics whose thickness varies azimuthally and thus possess a discontinuity in the thickness at $\phi = 0$. It is this azimuthal thickness variation that induces the $2\pi\ell$ azimuthal phase change. These optics do not create a pure mode, and are unable to transform a Gaussian beam into an $LG_{p>0}^\ell$ mode.

Computer generated holograms (CGH's) can be used to create higher $p$ laser modes [29, 10]. They are created by calculating the interference pattern expected between the incident mode and the desired mode. This pattern is then printed onto a diffraction grating. For modes with $p > 0$, there is a circular discontinuity in the pattern of the hologram. The resulting output of these holograms is a diffraction pattern with each diffraction order comprising modes of a single $\ell$, but a superposition of all $p$, with the majority of the intensity in the desired $LG_p^\ell$ mode. Arlt *et al* determine that the theoretical maximum mode purity possible for an $LG_1^1$ laser mode using CGH's is 80% of the intensity in the desired mode, which has been achieved experimentally [10]. This mode purity is determined by the ratio of the beam radius, $w_{beam}$, to the radius of the circular discontinuity in the pattern of the hologram, $w_{holo}$. For an $LG_1^1$ laser mode the maximum mode purity occurs when $w_{beam}/w_{holo} \approx 2$.

We create $LG$ beams with diffractive optics manufactured by Diffractive Optics Corporation (DOC). DOC etches small-scale (0.5 microns) structures on optical elements using state of the art photolithographic techniques. These microstructures diffract an incident wavefront yielding a beam profile that is a superposition of the

diffracted waves. Each $LG_p^\ell$ mode created requires two optics: one to control the intensity distribution and the other to fix the phase. The mode purity of beams created using these optics is limited only by the resolution of the lithographic techniques used to create the optics. We have optics to generate five different $LG_p^\ell$ modes: $LG_0^1$, $LG_1^2$, $LG_2^3$, $LG_0^5$, and $LG_1^{10}$ modes. 2D CCD intensity distribution images of these beams are shown in figure 3.2.

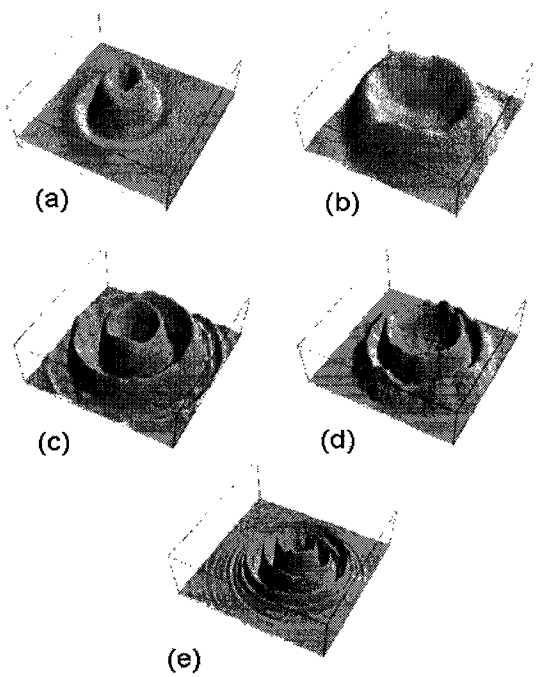



Figure 3.2: 2D intensity profiles of unoptimized $LG$ beams created using our diffractive optics taken with a CCD camera: (a) $LG_0^1$, (b) $LG_0^5$, (c) $LG_1^2$, (d) $LG_1^{10}$, and (e) $LG_2^3$. The external ring is (a), (c) , and (e) is due to diffraction from the edge of the optic

We begin with the output of a diode laser at 780 nm in the master oscillator power amplifier (MOPA) configuration. In this configuration, 5 mW laser power from a diode laser can be amplified up to 500 mW. We typically achieve amplified powers greater than 350 mW. Like a diode laser, the output of a MOPA is astigmatic.

We symmetrize this output using cylindrical lenses and then pass the beam through an optical isolator. The optical isolator acts as an optical diode and minimizes reflections back into the laser. The mode purity of our $LG_p^\ell$ laser beam is dependent upon the purity of the Gaussian beam incident upon the optics. In order to maximize the resulting mode purity we telescope the output of the optical isolator and direct into a single mode optical fiber to filter the beam. For these studies, we require very little power and therefore do not spend much time optimizing the alignment of the laser into the fiber. We typically obtain a 10 mW pure Gaussian laser mode out of the fiber. We then telescope the beam to an $e^{-2}$ beam radius of 0.5 mm, which is the optimal size of beam to be used with our optics.

DOC manufactured the optics with the specifications that the two optics must be placed 15.0±0.2 mm apart and have a relative tilt angle of less that ±3 arc min along any axis. The two optics are placed in a hollow cylindrical aluminum holder, 15 mm long, 12.5 mm inner diameter, and 25.4 mm outer diameter with four alignment pins on each end. The alignment pins are designed such that a corner of the square optic will fit between two alignment pins. There are two such sets of pins on each side of the holder for diagonal corners of the optics to fit between. A picture of this holder is shown in Figure 3.3. This holder is placed into a 1" mirror mount, which allows us to adjust the tilt angle of the optic relative to the incoming beam. The 1" mirror mount is attached to a 2D translation stage to adjust the position of the optics so that the beam will pass through the center of the optics. The transformed beam is then directed onto a CCD camera. A real time intensity distribution acquired from

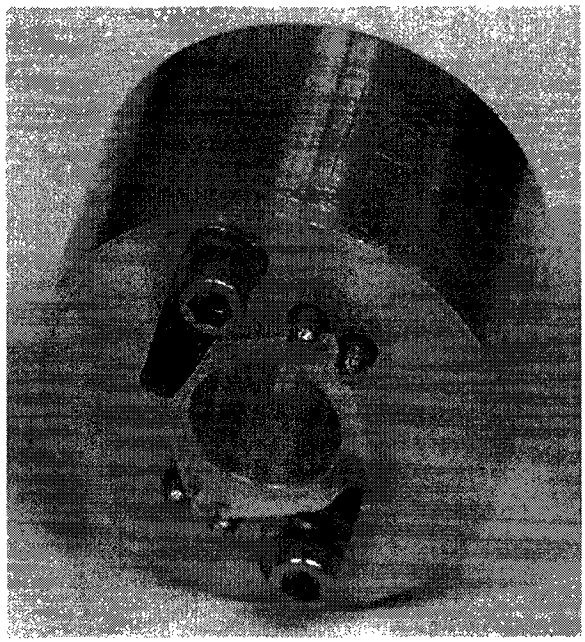


Figure 3.3: This is a picture of the holder designed to hold the diffractive optics. The optics are etched onto glass substrates, which are placed in the holder and aligned with the pins. The optics are held in place with small copper brackets.

the camera using a frame grabber installed in a PC running LabVIEW. This real time intensity distribution allows us to optimize our optics.

## 3.4 Laguerre-Gaussian beam analysis

In this section, I present detailed analysis of our $LG_0^1$ and $LG_1^2$ laser beams, including mode purity, conversion efficiency, and extinction ratio. I also present a comparison of our results with those published using computer generated holograms and spiral phaseplates, which is shown in Table 3.4.

The CCD camera, although handy for a real time image of our beams, does not have the resolution required to obtain an accurate radial intensity distribution. For

this we employed a manual method using a 10 $\mu$m pinhole on a translation stage and a photodiode amplifier circuit to measure the radial intensity distribution for two of our modes: the $LG_0^1$ and the $LG_1^2$ modes. We first focus the beam onto the photodiode, and then place the pinhole in the image plane of the optics (15 mm from the second optic). We are able to measure the intensity of the beam at the position of the pinhole by reading the voltage applied to an analog input channel of a data acquisition card using LabVIEW.

As we want a radial distribution, we need to be sure that we begin at the center of the beam. To do this, we monitor the output of the photodiode circuit and move the translation stage horizontally to find the position of the two maxima (the intensity peaks at either side of $r = 0$). We then position the translation state at the mid point of these maxima and repeat the process moving the translation stage vertically. The midpoint of the maxima in both the horizontal and vertical directions should represent the midpoint of the beam, $r = 0$. We then measure the output of the photodiode circuit as we increase the radius at which the pinhole is located. We subtract the background due to ambient light and scattered laser radiation. We repeat the process of placing the pinhole at the image plane, locating the center of the beam, and measuring the intensity distribution several times in order to randomize the errors introduced in the initial setup of the experiment. These errors are the dominant sources of errors. The average and standard deviation of the intensity are calculated at each point measured along the radius. The experimental intensity distributions of our $LG_0^1$ beam and our $LG_1^2$ beam are shown in Fig. 3.4 and Fig.

3.5 respectively, where the squares are the data and the line represents a theoretical fit to the data.

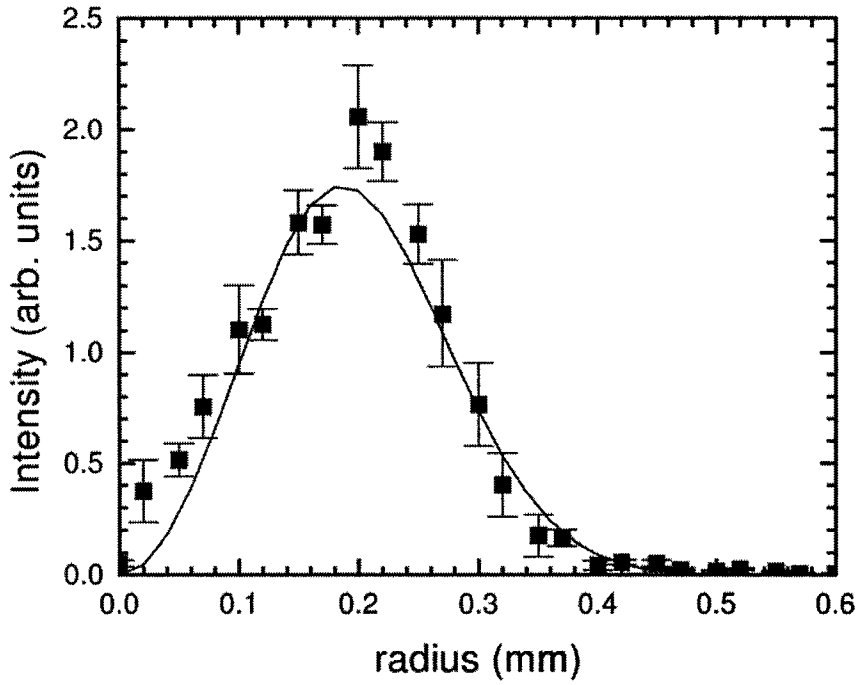



Figure 3.4: The intensity distribution of an $LG_0^1$ beam. The squares are the experimental measurements with the error bars representing one standard deviation. The line is the theoretical curve that shows >92% of the intensity in the $LG_0^1$ mode.

The extinction ratio, a measure of how dark the central node is, is determined by dividing the intensity measured at the central node by the intensity measured at the first intensity peak. This is an important figure of merit, as we want to trap atoms in the intensity node where effects such as the AC Stark shift are minimized. We measured extinction ratios of $(2.5\pm0.8)\times10^{-2}$ for the $LG_0^1$ beam and $(3.3\pm0.8)\times10^{-2}$ for the $LG_1^2$ beam. These high extinction ratios are illustrated in figures 3.4 and 3.5, where the greatest variation between the measured and theoretical intensity

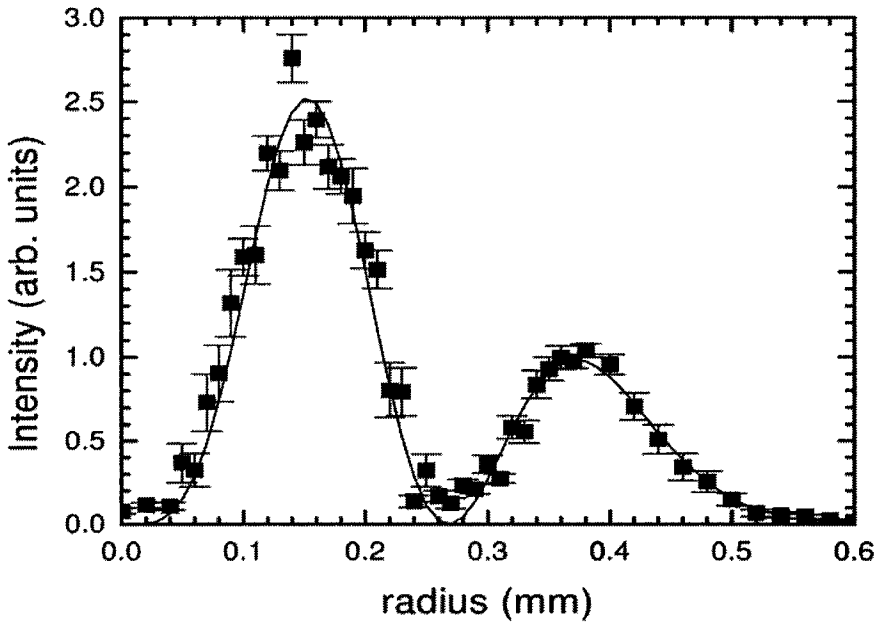



Figure 3.5: The intensity distribution of an $LG_1^2$ beam. The squares are the experimental measurements with the error bars representing one standard deviation. The line is the theoretical curve that shows >99% of the intensity in the $LG_1^2$ mode.

distributions is at the nodes, where the intensity is supposed to go to zero. We do not know of extinction ratios measured for $LG$ beams created using other methods.

The conversion efficiency is the ratio of power in the $LG$ mode of interest to that of the incoming Gaussian beam. For intracavity methods of creating $LG$ beams, where the only loss is a due to a decrease in gain, a similar figure of merit is the ratio of power in the $LG$ beam to that of the fundamental mode of the laser. We determine this by measuring the power of the laser before and after the $LG$ optics. We determine conversion efficiencies of greater than 40% for our $LG_0^1$ mode, and greater than 60% for our higher order modes. Computer generated holograms have a demonstrated conversion efficiency of 40% for higher order modes [10, 30].

The mode purity is the amount of intensity that is in the desired $LG_p^\ell$ mode. Unlike the other external cavity methods of creating $LG$ modes, we do not expect our beams to be a superposition of all $p$ modes. However, so that we can compare the quality of our beams with others, we model our intensity distribution in the same manner as Arlt *et al* [10] and let non-zero amplitudes in the other $p$ modes account for systematic errors. We do a rigorous $\chi^2_\nu$ calculation to fit the intensity distribution to a function given by $f^*f$, where $f = \sum_p c_p u_p^\ell$. The $c_p$ are numerical coefficients normalized such that $\sum_p c_p^2 = 1$, and $u_p^\ell$ is given by Equation 3.1.

We determine $\chi^2_\nu$ as follows [31]:

$$\chi^2_\nu = \sum_i \left( \frac{data_i - model(r_i, P, w, c_0, c_1, ...)}{\sigma_i} \right)^2, \tag{3.2}$$

where $data_i$ is the intensity measured with the pinhole at a radius $r_i$, and $\sigma_i$ is the standard deviation at that point. The model that we are fitting the data to is $model(r_i, P, w, c_0, c_1, ...) = f^*f$. The parameters $P, w, c_0, c_1, ...$ are independent parameters that are varied in order to minimize $\chi^2_\nu$. We begin by assuming that our beam is an ideal $LG_p^\ell$ mode. We vary the parameters $P$ and $w$ to minimize $\chi^2_\nu$. If $\chi^2_\nu$ is greater than 1, we add another $p$ mode, which adds another parameter, and again minimize $\chi^2_\nu$. We continue to add additional $p$ modes until $\chi^2_\nu$ no longer decreases and is nearly equal to 1. The mode purity of the $LG_{p_o}^\ell$ beam is then given as $c^2_{p_o}$. Using this method, we determine our $LG_0^1$ laser beam to have a mode purity of $92.9 \pm 2.9\%$. The mode purity of our $LG_1^2$ beam is $99.3 \pm 0.9\%$ which is consistent, within the error, with 100% of the intensity in the $LG_1^2$ laser mode.

Table 3.1: Comparison of $LG_p^\ell$ beam characteristics using different construction methods.

| Creation Method | Spiral Phaseplates | | Computer Generated Holograms | | | | Diffractive Optics | |
|---|---|---|---|---|---|---|---|---|
| $LG$ mode | $LG_0^1$ | $LG_0^2$ | $LG_0^1$ | $LG_0^3$ | $LG_0^6$ | $LG_1^1$ | $LG_0^1$ | $LG_1^2$ |
| Mode Purity | **78.5%** | 50% | **93%** | 77% | 62.8% | 80% | **92.9%** | 99.3% |
| Conversion Efficiency | | | | | | 40% | 40% | 60% |
| Extinction Ratio | | | | | | | $(2.5 \pm 0.8) \times 10^{-2}$ | $(3.3 \pm 0.8) \times 10^{-2}$ |

We also look at the $LG$ beams as they propagate from the image plane of the optics in order to further explore the possible application of these beams as atom traps. The method in which these beams are created generates an $LG_p^\ell$ mode in a plane 15 mm from the second optic. We therefore do not necessarily expect the beams to maintain their features as they propagate from this plane. Figures 3.6 and 3.7 show our $LG_0^1$ and $LG_2^3$ laser beams at several distances from the image plane. Figure 3.6(a) shows the $LG_0^1$ laser beam at 75 mm from the image plane. In this image there is a prominent extra ring around the central node that occurs from light diffracting around the edge of the optic itself. These diffraction rings diverge more quickly than the beam itself and the extra ring is no longer noticeable at 200 mm (Fig. 3.6(d)). The Figure also shows that as the beam propagates, it retains the central node. A true $LG$ mode should retain the central node due to the quantized orbital angular momentum. The fact that our beam does maintain its qualitative features is evidence that the optics are indeed creating a pure $LG_0^1$ laser mode. Figure 3.7 shows CCD images of an $LG_2^3$ laser beam created with diffractive optics. The general features of the mode (2 radial nodes and the central node) remain as

the beam propagates, although the relative peak intensities of the antinodes change as the propagation distance increases. There is an azimuthal asymmetry in the antinodes that increases as the beam propagates. This asymmetry may be due to a misalignment in the optics. The original mode purity may be recaptured by imaging the beam, but imaging may not be necessary if only the general features of the beam are required. Again, the fact that the central node remains is evidence that the optics are in fact creating a pure $LG_2^3$ laser mode.

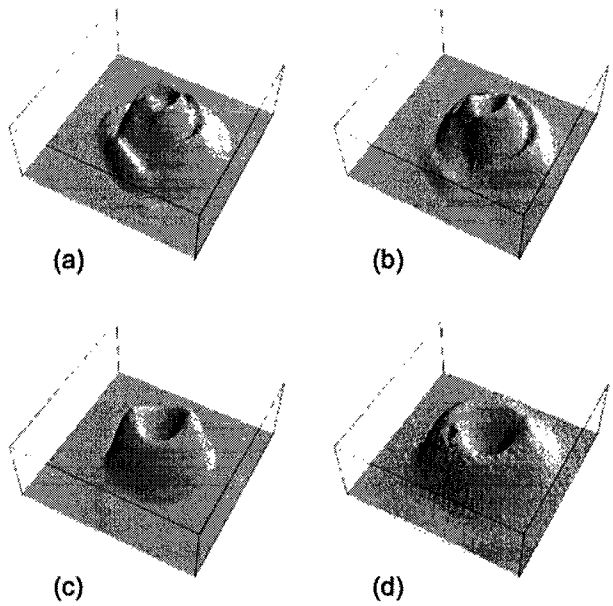



Figure 3.6: CCD images of an $LG_0^1$ laser beam as it propagates from the image plane. (a)75 mm, (b)100 mm, (c)150 mm, (d)200 mm. The additional ring in (a)-(b) occurs from light diffracting around the edge of the optic itself. This additional ring diffracts more quickly than the beam itself and is no longer visible in (d).

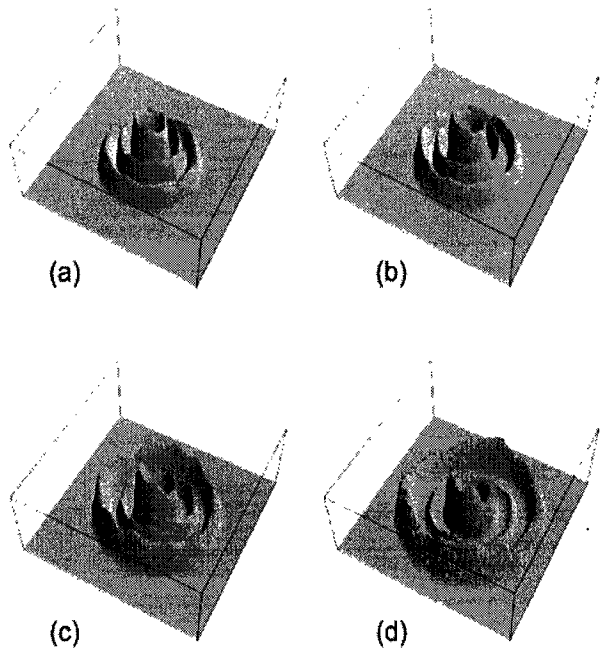



Figure 3.7: CCD images of an $LG_2^3$ laser beam as it propagates from the image plane. (a)75 mm, (b)100 mm, (c)150 mm, (d)200 mm.

## 3.5 Conclusion

Laguerre-Gaussian laser beams are used in several areas of atomic, molecular, optical, and solid-state physics due to their quantized orbital angular momentum and the radial nodes that they possess. While intracavity methods can make very pure higher order $LG$ beams, the use of diode lasers necessitates an external cavity method of creating $LG$ beams. Diffraction optics offer a means of making very pure Laguerre-Gaussian laser beams external to the laser cavity. Optics can be manufactured to transform a Gaussian laser beam into any desired $LG_p^\ell$ laser mode. The other external cavity method of creating higher order $LG$ laser beams is computer generated holograms. These holograms, unlike diffraction optics, produce a beam with the

desired $\ell$, but a superposition of all $p$ modes. The best possible mode purity that one can expect for an $LG_1^1$ laser mode created with computer generated holograms is 80% which has been achieved experimentally. We do not expect our beams to be a superposition of $p$ modes, but we analyze our laser beams as such so that systematic errors will show up as non-zero amplitudes in the other $p$ modes. We analyze two of the $LG$ beams that we are able to create using the optics that we possess. We determine mode purities of 93.9% for our $LG_0^1$ mode and 99.3% for our $LG_1^2$ mode. The $LG_1^2$ laser mode is consistent with 100% of the intensity in the $p = 1$ mode. We measure extinction ratios of $\sim 10^{-2}$, and the conversion efficiencies of our method are comparable to those using other external-cavity methods. We also look at the propagation characteristics of an $LG_0^1$ beam and an $LG_2^3$ mode. The general feature of the $p + 1$ radial nodes remain as the beam propagates, although the relative intensities of the antinodes in the $LG_2^3$ mode change as the propagation distance increases.

# Chapter 4

# Confinement of Atoms in a Laguerre-Gaussian Laser Beam

## 4.1 Introduction

The optical dipole force can either attract or repel atoms from the high-intensity regions of laser fields. At large detuning the optical dipole force potential is $U(r) = \frac{\hbar\Omega^2}{4\Delta}$, where $\Omega^2 = \frac{I(r)}{I_s}$ is the Rabi frequency squared, $I(r)$ is the intensity distribution of the laser, $I_s$ is the saturation intensity, and $\Delta$ is the detuning of the laser from resonance [32, 7]. If the laser is tuned below resonance (red-detuned) then the atoms are attracted to the high-intensity regions. If instead the laser is tuned above resonance (blue-detuned) then the atoms are repelled from the high-intensity regions.

Laguerre-Gaussian laser beams ($LG_p^\ell$), discussed in detail in Chapter 3, are laser modes with an azimuthal phase change of $e^{-\imath\ell\phi}$, a quantized orbital angular momentum of $\ell\hbar$ per photon, and $p+1$ radial nodes with $\ell > 0$. Ultra cold atoms trapped in the nodes of $LG$ laser beams may be useful for atomic clock studies as ac-Stark

shifts are minimized by trapping atoms in the low intensity regions [12]. Vortices in BECs trapped in the nodes of higher-order $LG$ beams may be observed using matter-wave interference [17] and ring shaped BECs in $LG$ beams can be used as rotational gyroscopes [18].

## 4.2 Experimental Setup

Our experiment to confine $^{87}$Rb atoms in an $LG_0^1$ laser beam begins with cooling and trapping the atoms in a vapor cell magneto-optical trap (MOT). The construction of the MOT is detailed in Chapter 2. The 30 mW $LG$ beam is created by transforming the Gaussian output of a spatially filtered diode laser in the MOPA configuration (Section A.5) using diffractive optics as described in Chapter 3. A shutter is placed in front of the diffractive optics so that the $LG$ beam can be turned on and off. The probe is the output of another diode laser, and it is shuttered using an acoustic optic modulator (AOM). Both the $LG$ beam and the probe are directed through $\lambda/2$ plates and then sent through a polarizing beam-splitter cube (PBC). A schematic of the experimental setup is shown in Figure 4.1. The two beams are collinear after exiting the PBC and are directed vertically through the MOT. After passing through the MOT, the beams are directed through a shutter and into a CCD camera. The very intense light from the $LG$ beam saturates our camera and thus it is important that the camera's shutter is opened only when the $LG$ beam has been turned off. Another shutter is placed in the beam path of the repump. When this shutter is closed, the atoms from the MOT are optically pumped into the $2S_{1/2}, F = 1$ state.

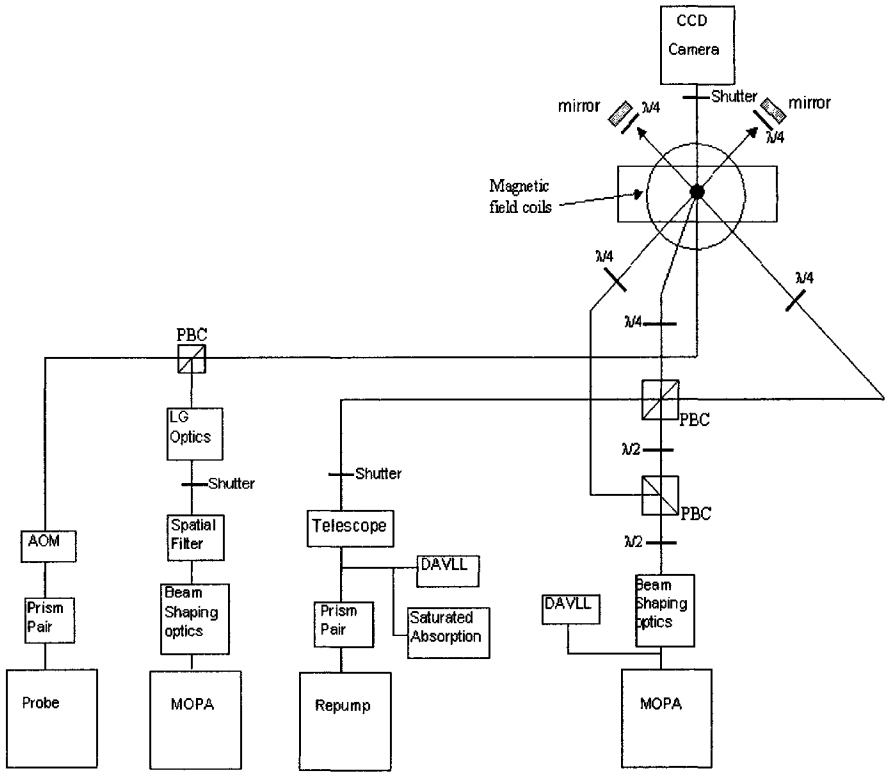



Figure 4.1: A schematic of the experimental setup for the confinement of atoms in an $LG$. The $LG$ beam is created from the spatially filtered output of a diode laser in the MOPA configuration using diffractive optics. The $LG$ beam is collinear with a probe and is directed vertically through the MOT and into a CCD camera.

## 4.3 Confinement of atoms in a blue-detuned $LG_0^1$ laser beam

We confine $\sim 10^7$ atoms in the central node of an $LG_0^1$ laser beam detuned 2 GHz above the $2S_{1/2}, F = 1 \rightarrow 2P_{3/2}, F' = 2$ transition. The timing for the experiment is computer controlled through LabView. A MOT containing $\sim 10^9$ atoms is created in a vapor cell as described in Chapter 2. The $LG$ beam is directed vertically through the bottom side of the glass cell and superimposed over the MOT. The experiment begins with closing the shutter through which the repump passes. This optically pumps the atoms into the $2S_{1/2}, F = 1$ hyperfine level. The $LG$ beam is

then shut off after some delay, which is varied. The shutter in front of the camera is opened 0.1 ms after the $LG$ beam has been turned off. This delay ensures that the $LG$ beam does not enter and saturate our camera. The probe, tuned to the $2S_{1/2}, F = 1 \rightarrow \ 2P_{3/2}, F' = 2$ transition, is flashed 1.9 ms later. This delay is necessary to ensure that the camera's shutter is completely open before the probe is flashed. The cloud of atoms absorbs light from the probe, and the shadow of the cloud is imaged onto the CCD camera.

The timing sequence is repeated without first collecting atoms in the MOT to normalize the absorption image obtained above. The resulting image has a value between 0 and 1 in each pixel, given by $e^{-\sigma n}$, where $\sigma$ is the scattering cross-section and $n$ is the column density. CCD pixels with a value of 1 correspond to areas where no atoms are confined. The number density obtained is fit to a Gaussian curve from which the size of the atom cloud is determined.

If atoms are confined to the node of our blue-detuned $LG_0^1$ beam then these atoms will not leave the low-intensity region until the $LG$ beam is turned off. To determine if atoms are confined to the node of the beam we vary the delay between turning the repump and the $LG$ beams off. If the atoms are confined to the node of the beam we should see little change in the size of the cloud as the delay is increased. If, however, the atoms are not confined to the node of our $LG$ beam then the size of the cloud will increase according to its temperature as the delay between turning the repump and the $LG$ beams off increases. We repeat the experiment without first superimposing the $LG$ beam over the MOT to verify that the cloud expands as expected when the atoms are not confined to the node of the $LG$ beam.

Figure 4.2 shows the $1/e$ radius of the atom cloud as the delay time is increased. The triangles represent the size of the atom cloud when the $LG$ beam is superimposed over the MOT. The size of the cloud remains fairly constant as the delay time is increased as expected for atoms confined in the node of the $LG$ beam. The squares in Figure 4.2 represent the size of the atom cloud when the $LG$ beam is not first superimposed over the MOT. In this case, the atom cloud when the atoms are not confined to the node of the $LG$ beam expands at a rate consistent with a temperature of 3 mK.

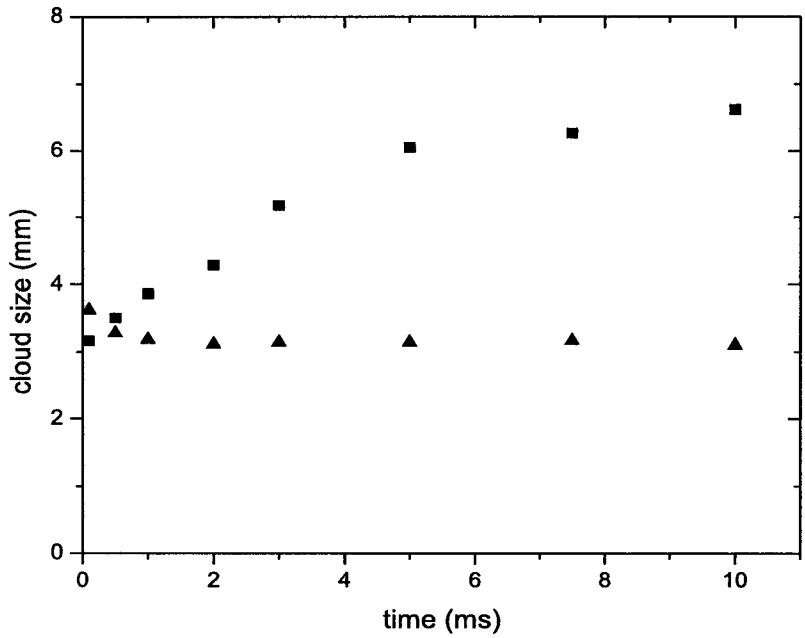



Figure 4.2: $1/e$ radius of the atom cloud as the delay between turning the repump and the $LG$ beams off increases. The squares represent the atom cloud from the MOT. The triangles represent the size of the cloud of atoms confined in the central node of a blue-detuned $LG_0^1$ laser beam. Because the atoms are confined, the size of the cloud remains the same as the delay is increased.

## 4.4 Confinement of atoms in a red-detuned $LG_0^1$ laser beam

We have confined 3 x $10^7$ atoms in the anti-node of a $LG_0^1$ laser beam tuned ~2 GHz to the red of the $2S_{1/2}, F = 2 \rightarrow 2P_{3/2}, F' = 3$ hyperfine transition. The $LG$ beam is collinear with a probe and directed vertically through the bottom face of our rectangular glass cell. The experiment begins by turning the $LG$ beam off. The camera shutter is then opened and the probe beam is flashed. Unlike the experiment in which we confine atoms to the central node of a blue-detuned $LG$ beam described in Section 4.3, in this experiment the repump beam is not turned off. This means that there are atoms confined within the MOT that are not confined to the high-intensity region of the $LG$ beam. The trap depth of this configuration is about 0.25 mK.

When the probe is flashed, the atoms in its path absorb photons. The number of atoms that the probe passes through can be obtained from a CCD image of the probe. Figure 4.3 shows the number density of atoms obtained with the red-detuned $LG$ beam superimposed over the MOT. In this figure, lighter colors represent areas with greater numbers of atoms. There is an area of greater atom density in a ring around the center of the distribution. This shows that atoms are being attracted to the high-intensity region of the $LG$ beam.

If all of the atoms in the system were confined to the high-intensity regions of the $LG$ beam the center of the cloud would be nearly void of atoms. However, the

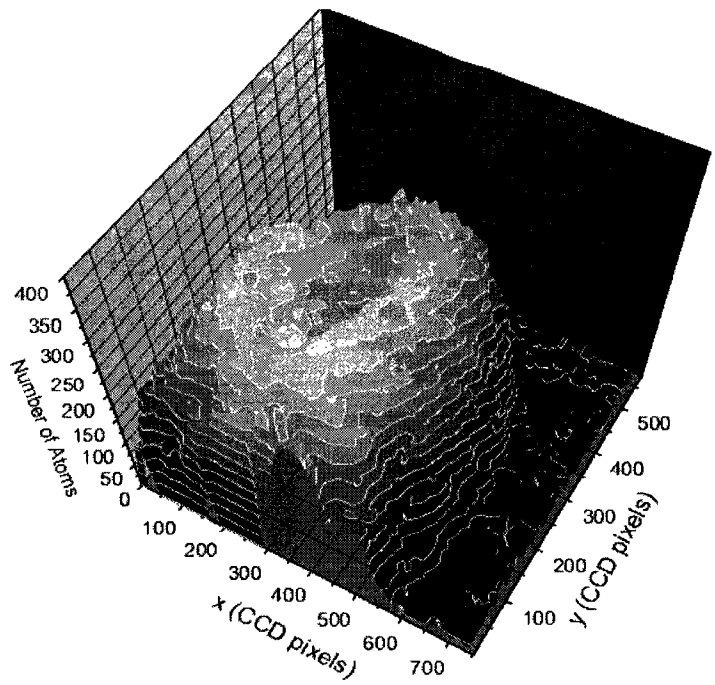



Figure 4.3: This figure shows the number density of atoms derived from the absorption image of the MOT with a red-detuned $LG_0^1$ beam superimposed over it. Lighter colors represent areas with greater numbers of atoms. In this figure, a ring around the center of the cloud contains a greater number of atoms than are located at the center. It is evident, then, that the atoms are being attracted to the high-intensity region of the $LG_0^1$ laser beam.

MOT was not shut off in this experiment, and there are still atoms within the system that are not confined to the $LG$ beam. In Figure 4.4 the Gaussian distribution of these atoms has been subtracted from the data shown in Figure 4.3. The density distribution shown in Figure 4.4 is only those atoms that have been confined to the high-intensity region of the $LG$ beam.

Cross sections of the atom cloud with the superimposed red-detuned $LG$ beam are shown in figure 4.5. The top figure shows the atom distribution including those atoms that are confined to the MOT but are not confined to the high-intensity region of the $LG$ beam. The squares are the data and the solid line is a fit to the data. The model used to fit the data consists of a central 3D Gaussian distribution that

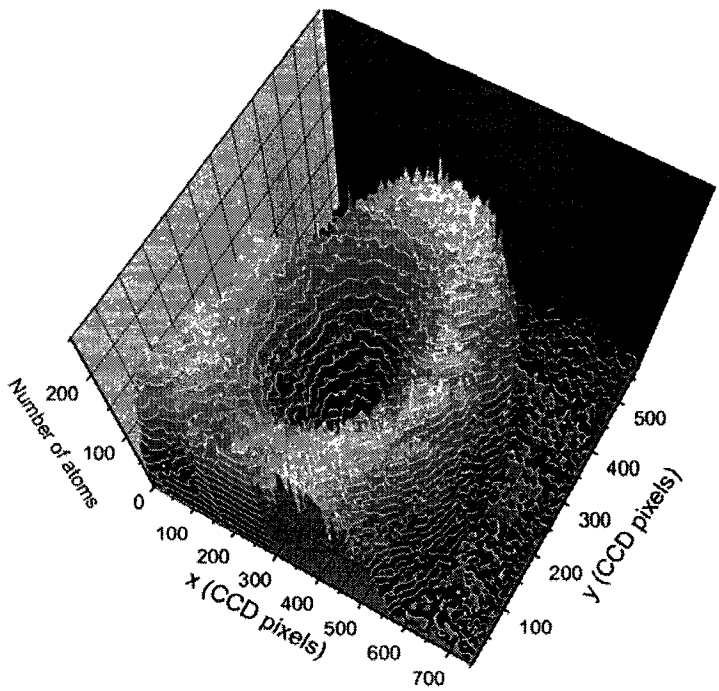



Figure 4.4: The number density of the atoms confined within the *LG* beam. In this figure, the Gaussian profile of the atoms confined within the MOT, but not confined to the high intensity region of the *LG* beam has been subtracted out.

represents the atoms in the cloud that are not confined to the *LG* beam. A second Gaussian distribution located at a radius $R$ and rotated about the $z$-axis represents those atoms that are confined to the *LG* beam. The solid line is obtained with a central Gaussian $1/e$ radius of 1.3 mm. The second Gaussian distribution is located at a radius of 1.5 mm and has a $1/e$ radius of 0.90 mm.

The bottom figure is a cross-section that is perpendicular to the cross-section shown in the top figure. In this figure the atoms not confined to the *LG* beam have been subtracted. It is evident that there are a greater number of atoms on one side of the node. This is due to an asymmetry in the intensity profile of the *LG* beam. It has been noted previously that small misalignments of the diffractive optics used

to create the beams causes these asymmetries [11]. Images of atoms confined to red-detuned $LG$ beams may then offer insight into the mode purities of the beams.

## 4.5 Conclusion

We have successfully demonstrated the confinement of $^{87}$Rb atoms loaded from a magneto-optical trap (MOT) in an $LG_0^1$ beam created with diffractive optics. For a laser tuned below resonance, the optical dipole force attracts to regions of high intensity laser fields. We tuned our $LG$ beam 2 GHz to the red of the $2S_{1/2}, F = 2 \rightarrow 2P_{3/2}, F' = 3$ transition and trapped $\sim$ 3 x $10^8$ atoms in the outer ring of the beam.

We also have confined atoms to the central node of an $LG_0^1$ beam tuned 2 GHz above the $2S_{1/2}, F = 1 \rightarrow 2P_{3/2}, F' = 2$ transition. Atoms confined in blue-detuned traps may be useful for atomic clock studies. In addition, BECs confined in the nodes of higher-order $LG$ beams may be used as rotational gyroscopes. In addition, vortices in BECs confined in higher-order $LG$ beams may be observed using matter wave interference.

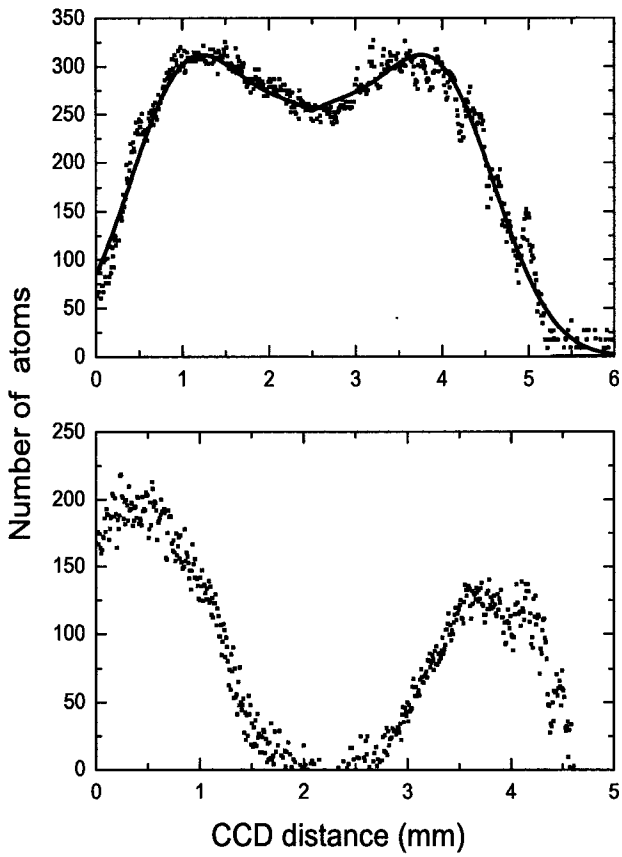



Figure 4.5: This figure shows cross-section of the data in Figure 4.4. The top figure shows a cross section of the data without the Gaussian profile of those atoms not confined within the high intensity region of the $LG$ beam subtracted. The data is fit to a model of a central Gaussian distribution with a second Gaussian distribution centered at a radius $R$ and rotated about the $z$-axis. The fit is shown as the solid line in the figure. The bottom figure is a cross-section perpendicular to that of the top cross-section. The asymmetry in the number density it due to an asymmetry in the intensity profile of the $LG$ beam caused by small misalignments in the diffractive optics.

# Chapter 5

# Properties of Bose-Einstein condensates in external potentials

## 5.1 Introduction

The transformation of a gas of atoms to a BEC is marked by the collection of particles in the ground state of the system below the critical temperature. This chapter describes how to calculate the critical temperature for experimentally realizable gasses in external potentials.

We consider an ideal gas of non-interacting bosons of mass $m$. The average number of particles in a state, $i$, with energy, $\varepsilon_i$, is [33]

$$n_i = \frac{1}{e^{\frac{\varepsilon_i - \mu}{kT}} - 1}, \tag{5.1}$$

where $\mu$ is the chemical potential. The total number of atoms in the system is then the sum of the atoms in all of the states

$$N = \sum_i n_i, \tag{5.2}$$

and the total energy of the gas is the sum of the energies of all of the particles

$$E = \sum_i \varepsilon_i n_i. \tag{5.3}$$

If we assume that the energy scale in which we are interested is large compared to the quantum scale, then the number of atoms can be calculated by

$$N = N_o + \int_0^\infty \rho(\varepsilon) n(\varepsilon) d\varepsilon, \tag{5.4}$$

where the density of states, $\rho(\varepsilon)$, is the density of quantum states at an energy $\varepsilon$. The number of particles in the ground state, $N_o$, must be explicitly added because $\rho(\varepsilon)$ is usually proportional to some power of energy, *i.e.* $\rho(\varepsilon) \propto \varepsilon^n$. Thus there is no contribution to the integral when $\varepsilon = 0$.

The total energy of the gas can be calculated in a similar matter:

$$E = \int_0^\infty \varepsilon \rho(\varepsilon) n(\varepsilon) d\varepsilon, \tag{5.5}$$

where we have assumed that the energy of the ground state is 0. The density of states is then needed in order to calculate the thermodynamic quantities.

The number of states in a volume, $d^3r$, that a particle with momentum between $p$ and $p + dp$ can occupy is:

$$\Omega(p)d^3\vec{r}dp = \frac{d^3\vec{r}d^3\vec{p}}{h^3} = \frac{d^3\vec{r}4\pi p^2 dp}{h^3}. \tag{5.6}$$

The energy of a non-interacting particle with momentum, $p$, in an external potential, $U(\vec{r})$, is:

$$\varepsilon(\vec{r}) = \frac{p^2}{2m} + U(\vec{r}) \tag{5.7}$$

The number of states with energy between $\varepsilon$ and $\varepsilon + d\varepsilon$ is then

$$\Omega(\varepsilon)d^3\vec{r}d\varepsilon = \frac{2\pi(2m)^{3/2}}{h^3}\sqrt{\varepsilon - U(\vec{r})}d\varepsilon d^3\vec{r} \tag{5.8}$$

The density of states is determined by integrating the above equation with knowledge of the external potential [34],

$$\rho(\varepsilon) = \frac{2\pi(2m)^{3/2}}{h^3}\int_{V^*(\varepsilon)}\sqrt{\varepsilon - U(r)}d^3r, \tag{5.9}$$

where the integral is taken over the spatial volume, $V^*(\varepsilon)$, that a classical particle with energy $\varepsilon$ can occupy.

A better understanding of can be obtained by examining the well-known case of the homogeneous ideal gas. In this case

$$\rho(\varepsilon) = \frac{2\pi V(2m)^{3/2}}{h^3}\sqrt{\varepsilon}. \tag{5.10}$$

The number of atoms in the gas is then, according to Equation 5.4

$$N = N_o + \frac{2\pi V(2m)^{3/2}}{h^3} \int_0^\infty \frac{\sqrt{\varepsilon}}{e^{\frac{\varepsilon-\mu}{kT}} - 1} d\varepsilon \tag{5.11}$$

Let us assume that $N_o = 0$ and examine what happens if we change the experimentally controllable parameters ($N$, $V$, and $T$). If we increase $N$, while holding $V$ and $T$ constant, then $\mu$ must increase for Equation 5.11 to still be satisfied. Similarly $\mu$ must increase if we decrease $V$ while keeping $N$ and $T$ constant, or if we decrease $T$ while keeping $N$ and $V$ constant. The chemical potential cannot be greater than 0. If we continue to change the experimentally controllable parameters as described above, in order for Equation 5.11 to continue to be satisfied particles must go into the ground state after $\mu$ has reached 0. When the temperature of the system is decreased while holding $N$ and $V$ constant, we can define the critical temperature, $T_c$, as the temperature at which $\mu = 0$ and $N_o = 0$. Below $T_c$, the particles condense into the ground state. For our homogeneous ideal gas this temperature is

$$T_c = \frac{h^2}{2\pi mk} \left(\frac{N}{V}\right)^{2/3} \zeta(3/2)^{-2/3}, \tag{5.12}$$

and the condensate fraction (the ratio of the number of atoms in the ground state to the total number of atoms in the gas) is

$$\frac{N_o}{N} = 1 - \left(\frac{T}{T_c}\right)^{3/2} \tag{5.13}$$

As shown in figure 5.1 there are no atoms in the ground state at $T = T_c$. As the temperature falls below $T_c$ the number of atoms in the ground state increases until all of the atoms are in the ground state at $T = 0$. From equation 5.12, it is also noted that at $T_c$

$$\left(\frac{N}{V}\right)^{1/3} = \zeta(3/2)^{1/3}\left(\frac{2\pi mkT_c}{h^2}\right)^{1/2} = \frac{1.37725}{\lambda_{dB}}, \tag{5.14}$$

where $\lambda_{dB}$ is defined as the thermal deBroglie wavelength. In other words, at the BEC transition, the thermal deBroglie wavelength is approximately equal to the interparticle spacing, $\left(\frac{V}{N}\right)^{1/3}$.

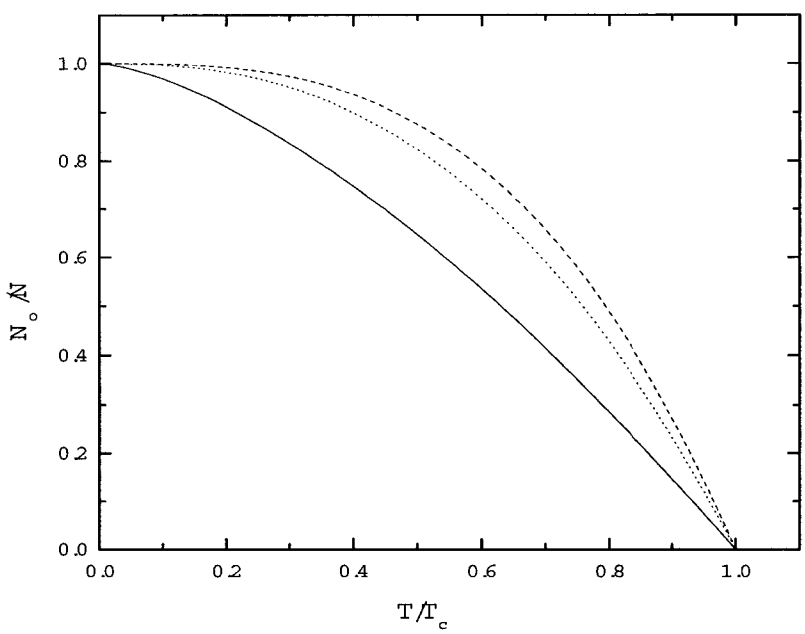



Figure 5.1: The number of particles in the ground state of a trap as the temperature approaches $T_c$. The solid line is the ideal gas in a 3D square well. The dashed line is a 3D simple harmonic oscillator potential, and the dotted line is the toroidal potential approximated as a rotated 2D simple harmonic oscillator potential.

## 5.2 Three Dimensional Simple Harmonic Oscillator

The 3D simple harmonic oscillator potential

$$U(r) = \frac{1}{2}m\omega^2 r^2 \tag{5.15}$$

is very important in BEC theory as most BEC's are formed in simple harmonic oscillator type traps [35]. The density of states is found using Equation 5.9 with the potential defined in Equation 5.15:

$$\rho(\varepsilon) = 4\pi\frac{2\pi(2m)^{3/2}}{h^3}\int_0^{r_{max}}\sqrt{\varepsilon - \frac{1}{2}m\omega^2 r^2}\, r^2 dr, \tag{5.16}$$

where the integral over the solid angle has already been done. A classical particle of energy, $\varepsilon$, can occupy a space such that $U(r) \leq \varepsilon$. Then, from Equation 5.15, the maximum radius is

$$r_{max} = \sqrt{\frac{2\varepsilon}{m\omega^2}}. \tag{5.17}$$

The density of states for the simple harmonic oscillator potential is then determined from Equation 5.16 integrated over the region defined in Equation 5.17:

$$\rho(\varepsilon) = \frac{\varepsilon^2}{2\hbar^3\omega^3}. \tag{5.18}$$

The number of atoms in the simple harmonic oscillator at a temperature, $T$ near $T_c$ is determined from Equation 5.4 using the density of states defined in Equation 5.18:

$$N(T) = N_o + \int_0^\infty \frac{\varepsilon^2}{2\hbar^3\omega^3} \frac{1}{e^{\frac{\varepsilon}{kT}} - 1} d\varepsilon \tag{5.19}$$

At $T_c$ there are no atoms in the ground state, so

$$N(T_c) = \frac{(kT_c)^3}{\hbar^3\omega^3}\zeta(3), \tag{5.20}$$

where the following definition has been used to evaluate the integral in Equation 5.19 [36]:

$$\zeta(x) = \frac{1}{\Gamma(x)} \int_0^\infty \frac{u^{x-1}}{e^u - 1} du. \tag{5.21}$$

$T_c$ is then determined to be:

$$T_c = \frac{\hbar\omega}{k} \left( \frac{N}{\zeta(3)} \right)^{1/3}, \tag{5.22}$$

and the condensate fraction is found from Equation 5.19 using the number of atoms found in Equation 5.20

$$\frac{N_o}{N} = 1 - \left( \frac{T}{T_c} \right)^3 \tag{5.23}$$

In figure 5.1 it is seen that the number of atoms in the ground state increases more rapidly for the gas in the simple harmonic oscillator potential than it does for the homogeneous ideal gas.

In real laboratory experiments atoms in the temperature regime of laser cooling and BEC are affected by gravity, as opposed to room temperature atoms where the effects of gravity are negligible. Adding gravity to the simple harmonic potential serves only to offset the zero of the potential in the $z$ axis. There is no effect of gravity on the density of states of the simple harmonic oscillator potential.

## 5.3 Toroid

We are interested in the properties of a BEC in a toroidal (donut) trap that may be provided with a light trap using Laguerre-Gaussian beam. A first model of such a trap is a 2-dimensional simple harmonic oscillator centered at a radius $R$ and rotated about the z-axis.

$$U(r,z) = \frac{1}{2}m\omega^2\left((r-R)^2 + z^2\right) \tag{5.24}$$

in cylindrical coordinates. As has been performed previously, the density of states is found from Equation 5.9 using the potential defined in Equation 5.24:

$$\rho(\varepsilon) = \frac{4\pi^2(2m)^{3/2}}{h^3}\int_{z_{min}}^{z_{max}}\int_{r_{min}}^{r_{max}}\sqrt{\varepsilon - \frac{m\omega^2}{2}\left(z^2 + (r-R)^2\right)}\,drdz, \tag{5.25}$$

where the angular integration has already been completed. The integral in equation 5.25 is evaluated over the volume that a classical particle with energy $\varepsilon$ can occupy:

$$-\sqrt{\frac{2\varepsilon}{m\omega^2} - (r-R)^2} \leq z \leq \sqrt{\frac{2\varepsilon}{m\omega^2} - (r-R)^2} \tag{5.26}$$

$$R - \sqrt{\frac{2\varepsilon}{m\omega^2}} \leq r \leq R + \sqrt{\frac{2\varepsilon}{m\omega^2}} \tag{5.27}$$

The density of states determined from Equation 5.25 using the integration limits defined in Equations 5.26 and 5.27 is:

$$\rho(\varepsilon) = \frac{4\sqrt{2}}{3} \frac{Rm^{1/2}\varepsilon^{3/2}}{\hbar^3\omega^2} \tag{5.28}$$

The critical temperature and the condensate fraction is found as in Section 5.2:

$$T_c = \left( \frac{\hbar^3\omega^2 N}{(2\pi m)^{1/2} R\zeta(5/2)} \right)^{2/5} \tag{5.29}$$

$$\frac{N_o}{N} = 1 - \left( \frac{T}{T_c} \right)^{5/2}. \tag{5.30}$$

As in the simple harmonic oscillator case, gravity only offsets the zero of the potential in the $z$ axis. There is no effect on the density of states.

## 5.4 Experimentally realistic toroid

A more experimentally realizable toroidal potential than the one considered in the previous section consists of a rotated simple harmonic oscillator potential provided perhaps by a blue-detuned higher-order Laguerre-Gaussian laser beam directed vertically through the glass cell. The confinement in the $z$ axis could be achieved with

a blue-detuned Gaussian laser beam directed horizontally through the cell below the cloud of atoms:

$$U(r,z) = \frac{1}{2}m\omega_r^2(r-R)^2 + Ae^{-z^2/w_z^2} + mgz + U_o, \tag{5.31}$$

where $A = \frac{\hbar\Omega^2}{4\Delta}$, $w_z$ is the beam waist, $\Omega$ is the Rabi frequency, and $\Delta$ is the detuning. $U_o$ is chosen such that $U(R, z_o)$=0, where $z_o$ is the location of the potential minimum.

Unfortunately, the density of states for the above potential is not analytically solvable. As an approximation, we Taylor expand the $z$ dependent portion of the potential about $z_o$:

$$U_{approx}(r,z) = \frac{1}{2}m\omega_r^2(r-R)^2 + \frac{1}{2}m\omega_{z_{eff}}^2(z-z_o)^2, \tag{5.32}$$

where $\frac{1}{2}m\omega_{z_{eff}}^2 = \frac{mgz_o}{w_z^2} - \frac{Ae^{-z_o^2/w_z^2}}{w_z^2}$. Then, the potential is the same as that of a rotated harmonic oscillator potential, and the density of states is similar to Equation 5.28:

$$\rho(\varepsilon) = \frac{4\sqrt{2}}{3}\frac{Rm^{1/2}}{\hbar^3\omega_r\omega_{z_{eff}}}\varepsilon^{3/2} \tag{5.33}$$

We have used reasonable experimental parameters to compare our approximated potential with the actual potential in order to examine the validity of our approximation. The results of this comparison are shown in Figure 5.2. This figure shows that the approximation is fairly good near $z_o$, but quickly becomes less valid as $z$ increases or decreases. We have found that this approximation is not valid and further numerical evaluation of the potential is necessary.

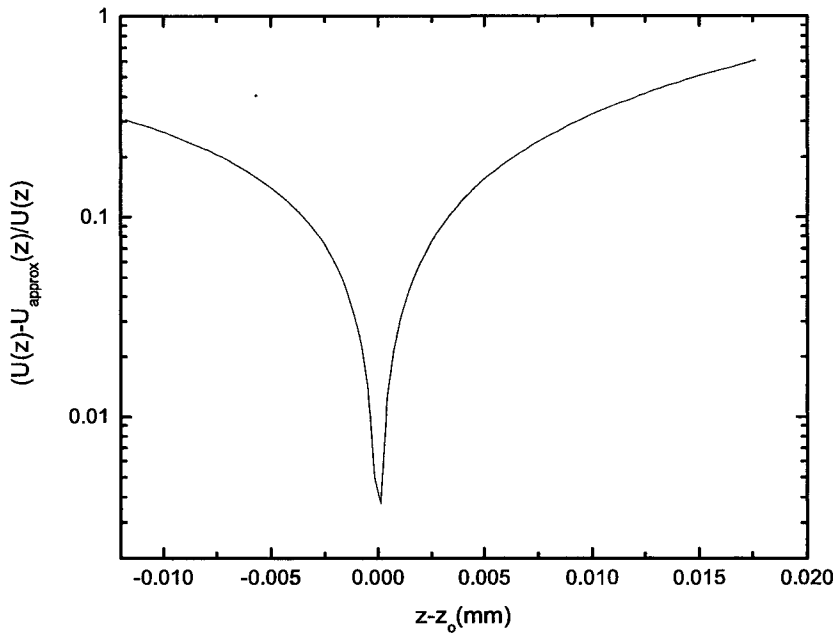



Figure 5.2: This figure shows a comparison of the toroidal potential in a gravitational field supported by a blue-detuned laser beam described in Equation 5.31 with the second order approximation to that potential described in Equation 5.32. The approximation is good at $z_o$, but quickly becomes less valid as $z$ increases or decreases.

# Chapter 6

# Conclusion

Atom traps created from Laguerre-Gaussian ($LG$) laser beams could be beneficial for atomic clock and Bose-Einstein condensation (BEC) studies. The most common external cavity method for creating these beams is with computer generated holograms. The observation of vortices in BEC using matter-wave interference requires that the atoms be trapped in a higher-order $LG$ beam. Higher-order $LG$ beams created with computer generated holograms results in a beam with the desired $\ell$ but a superposition of all $p$ modes. The majority of the intensity is in the desired $p$ mode, but the beam still in not a pure $LG$ mode. In collaboration with Digital Optics Corporation we have created pure higher-order $LG$ beams using diffractive optics. Detailed analysis of these beams is presented in Chapter 3. These optics allow us to create higher-order $LG$ modes with $> 99\%$ mode purity.

We directed a 30 mW $LG_0^1$ beam created with diffractive optics vertically through the cloud of atoms confined in our magneto-optical trap. A probe directed collinearly with the $LG$ beam is used for absorption imaging. With this configuration, described

in Chapter 4, we have observed $10^7$ atoms trapped in the central node of a blue-detuned $LG$ beam. We have also observed atoms trapped in the high-intensity region of a red-detuned $LG$ beam. An asymmetry in the absorption profile of the atoms confined in the red-detuned $LG$ beam was observed corresponding to an asymmetry in the intensity profile of the $LG$ beam that has been observed previously.

As a BEC trapped in these beams is experimentally interesting, we attempt to calculate the transition characteristics of an experimentally realizable potential in Chapter 5. We approximate the potential with a second-order Taylor expansion. The solutions to this are analytically solvable and are the same as that of a simple-harmonic oscillator potential rotated about the $z$-axis. However, this approximation is not valid through the entire BEC regime and further numerical evaluation is needed.

# Appendix A

# Diode Lasers

## A.1 Introduction

All of our experiments begin with a magneto-optical trap in an $^{87}$Rb vapor cell. In order to trap atoms in a magneto-optical trap lasers are needed with frequencies near the cycling transition, which in Rb is at 780 nm. This is fortunate as 780 nm also happens to be the wavelength near which laser diodes used in CD players operate. Thus, these laser diodes are mass-produced and are relatively inexpensive.

A diode laser alone will operate at a specific wavelength, which may be several nano-meters from the desired wavelenth. This frequency is only slightly tunable with current. An external cavity can be set-up by placing a grating in front of the laser output and reflecting one of the diffractions orders back into the laser for feedback. With an external cavity, diode lasers are made to be tunable and have a very narrow bandwidth. This makes them ideal for use in laser cooling and trapping. The disadvantages to these lasers are that they are highly static sensitive and small temperature changes can vary the frequency greatly. These lasers

also tend to become unstable in time, most likely due to small static discharges or power fluctuations although steps have been taken to minimize these effects. In this chapter, the procedures involved in building an external cavity diode laser are detailed. Much of this information can also be found in [37]. The construction of a Master Oscillator Power Amplifier (MOPA) is also explained.

## A.2 Construction of a diode laser

This section gives details of the construction of a diode laser from scratch. Most of the lasers needed have already been built and may need to have the diodes replaced in the future. For the purpose of diode replacement the reader should begin at section A.2.3. Figure A.1 is a picture of one of our finished lasers. Many of the parts used in the construction of the lasers are identified in this picture.

### A.2.1 Description of parts

Most of the parts required for the construction of a diode laser have been built by our machine shop. These parts include the aluminum heat sink block, the base plate, the flexure mount on which the laser diode and the collimation lens are mounted, the diode mount, the lens mount, and the aluminum lid. The other parts necessary are the laser diode itself, a diode holder, a mirror mount with hex head adjustments on which the grating is mounted, a 3/16" ultra-fine adjustment nut that goes into a 5/16" 32 thread tapped hole in the flexure mount and allows a 3/16" 100 thread precision screw to be used for fine adjustments, a power supply, a 8.18 mm focal

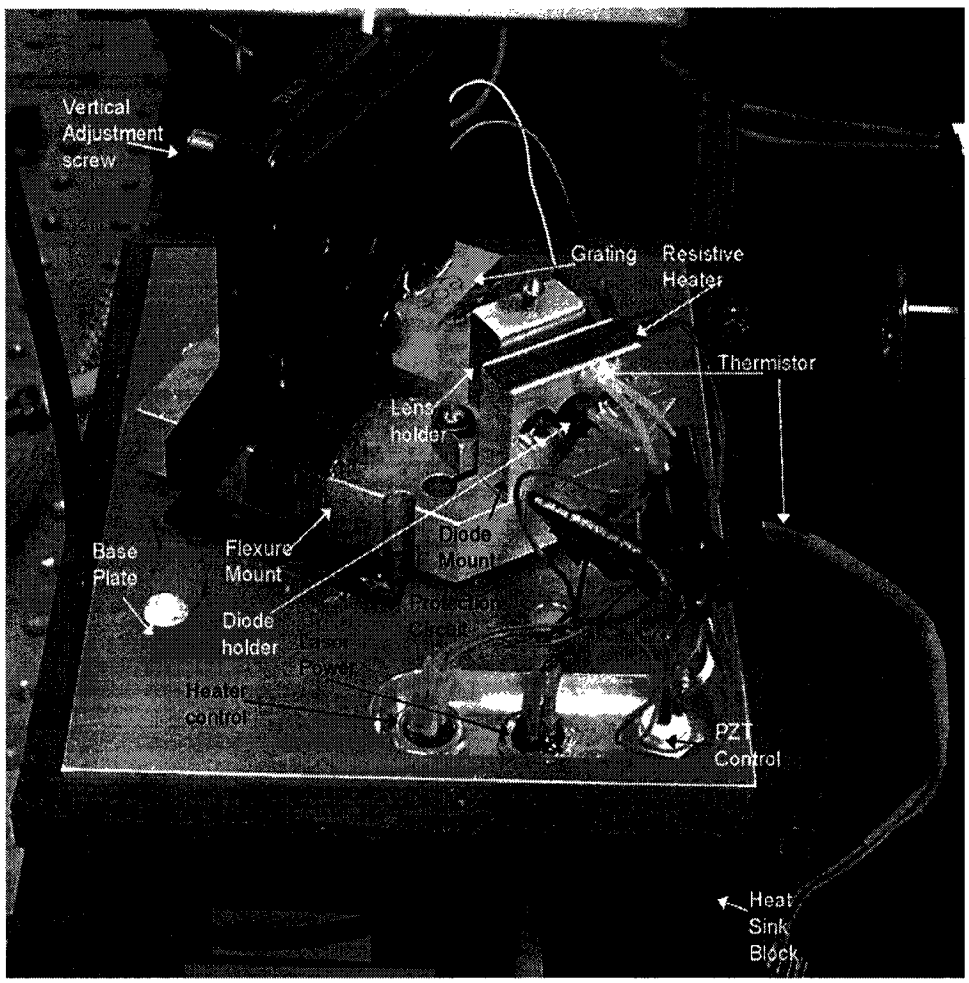



Figure A.1: A digital picture of one of our diode lasers. Many of the parts required in the construction of the laser are identified in this picture.

length lens that we purchase from Navitar, Inc., a 1200 lines/mm grating manufactured for operation at 750 nm, a thermo-electric cooler (TEC), a resistive heater, two thermistors, a piezoelectric transducer(PZT), three female 4 pin connectors, and a BNC connector.

The aluminum heat sink block is just that: a 5" x" 5 x" 5 aluminum block with four 8-32 tapped holes with which to mount the base plate. This block is used to dissipate the heat generated by the TEC. The base plate is a 6 5/8" x 5 1/2" aluminum plate with a lip around the perimeter on which the lid rests. There are

four countersunk holes in for mounting the base plate to the heat sink block. On one end there is a 2 1/2" countersunk area with three holes to mount two 4 pin connectors and the BNC connector. There is a small hole drilled into one side of the plate that holds a thermistor.

A schematic diagram of the flexure mount that holds the diode mount and the lens mount is shown in fig. A.2. The diode is mounted on one side of the flexing notch and the lens is mounted on the other. The precision screw is used to push against the flexing notch and minutely change the distance between the diode and the lens for laser collimation as described in section A.2.3.

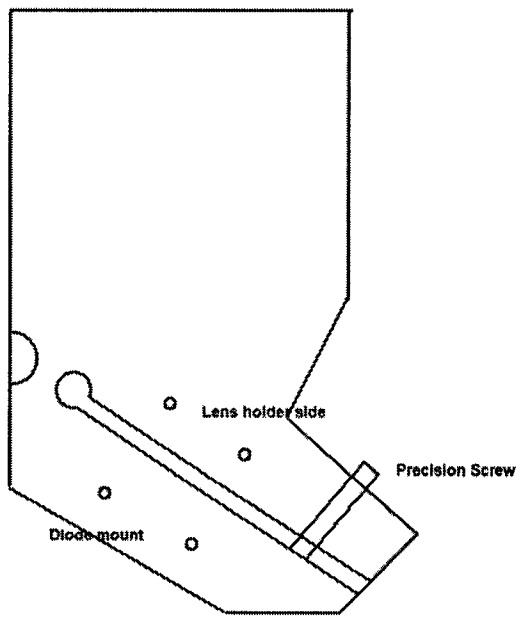



Figure A.2: Schematic of the flexure mount not drawn to scale. The precision screw pushes against the notch and minutely changes the distance between the diode and the lens when collimating the output of the diode laser.

The diode mount is a small 7/8" x 1 1/4" x 3/8" aluminum block with three countersunk holes drilled into it. The middle hole holds the laser diode and the two

tapped side holes hold washers with which the diode is secured. On the bottom of the block are two 4-40 tapped holes for mounting to the base plate. The lens mount is a block of aluminum with a hole in the center that holds the lens. The lens is secured with a setscrew from the top of the mount. There are milled slots on either side of the lens mount through which 4-40 screws mount the holder onto the base plate. These slots allow for a rough adjustment of the lens before the screws are fully tightened.

Laser diodes come in several different powers, wavelengths, and sizes. We have discovered when ordering laser diodes that although a diode may be listed as a 780 nm diode, the actual output may vary from this by more than 5 nm. Thor Labs, through whom we purchase our diodes, often allows us to request the output of the diodes to be within a desired range. We generally request that the output of our diodes not deviate from 780 nm by more than 3 nm. The setup that we use has been designed for a 9 mm can diode. The diode is placed into a diode holder, which is a small piece of plastic with three holes on one side to insert the diode and three pins on the backside that can be soldered to.

### A.2.2 Construction of the diode assembly

The first thing that is done in constructing the laser diode assembly is to attach the TEC to the heat sink. We apply thermally conductive double-sided tape manufactured by 3M (part# 9882) to both sides of the TEC. It is important that the heat side of the TEC is placed properly onto the heat sink before it is adhered, as the

tape is very strong and difficult to remove. The base plate is then placed on top of the TEC and attached to the heat sink block using nylon screws. A small amount of Thermalcote thermal joint compound manufactured by Termalloy, Inc. is applied to the tip of a thermistor which is placed in the hole drilled into the base plate and epoxied with 5 minute epoxy. Care is taken to ensure that not much thermal joint compound gets on the outside of the hole as it interferes with the curing of the epoxy. The thermistor and TEC leads are connected to a female 4-pin connector that hangs off the side of the base plate. The positive lead of the TEC (red wire) is connected to pin A, the negative lead is connected to pin B, and the two leads of the thermistor are connected to pins C and D. The remaining two 4-pin connectors and the BEC connector are bolted into the 3 holes drilled into the base plate.

The ultra-fine adjustment nut is inserted into the tapped hole on the flexure mount and the precision screw is screwed into the adjustment nut. The precision screw is inserted far enough into the adjustment nut to ensure that the mount is flexed to a small degree. This allows adjustments to occur while turning the screw clockwise or counter-clockwise.

The diode mount is attached to the flexure mount, and the resistive heater is attached to the top of the mount with the adhesive back. The second thermistor has thermal joint compound applied to it and is epoxied into the small hole near the top of the diode mount. The leads of the resistive heater are connected to pins A and B and the leads for the thermistor are connected to pins C and D of one of the 4-pin connectors bolted into the base-plate. A few pieces of vibration isolation

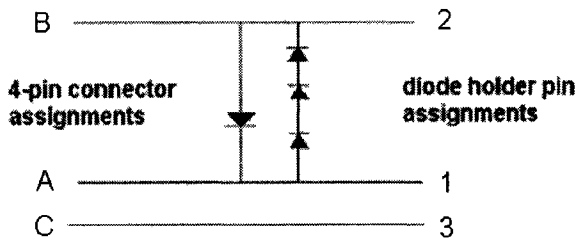



Figure A.3: This figure shows the protection circuit that is wired between the 4-pin connector connecting the power supply and the diode holder. The pin assignments for the convention used in our lab are given.

material are placed on the bottom side of the flexure mount, which is then just set onto the base plate.

### A.2.3 Diode mounting and collimation

Because the diodes are so extremely sensitive to static discharge and power fluctuations, a protection circuit is wired between the 4-pin connector and the diode holder. The schematic of the protection circuit is found in [37] and is also shown in figure A.3 along with pin assignments for the convention used in our lab. The diode holder has three pins that make a half circle. When held as shown in figure A.4 we will designate pins 1-3 starting from the top of the holder. The diode also has three pins in the same configuration and just slides into the holder.

The power cord between the power supply and the 4-pin connector is constructed and configured according to the power supply manual for the specific type of diode purchased. The diode is placed in the diode holder that then is placed into the mount and aligned as shown in figure A.4. This ensures that the output is nearly a horizontal line. Two 4-40 screws with washers are placed into the holes on either

side of the diode but are not tightened completely until power is applied to the diode and the output is observed on an infrared detection card. The diode is rotated until the output is a horizontal line and the screws are tightened after it has been verified that the washers are covering part of the diode.

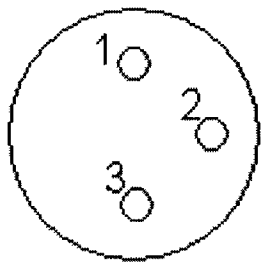



Figure A.4: This figure shows the back of the diode holder. The diode should be placed into the diode mount with the holder in the configuration shown. The output of the diode is then a horizontal line.

The collimation lens is placed into the lens holder and set with a 4-40 screw. The lens holder is then placed onto the flexure mount and two 4-40 screws loosely hold it in place while still allowing it to slide. The laser is roughly collimated by moving the lens holder back and forth by hand, and the lens holder is then firmly secured with the screws. It is necessary to check that the lens housing is not clipping the laser by observing the laser output with the IR detection card. The IR viewer is also useful for this purpose. The laser is then collimated more precisely using the adjustment screw in the flexure mount. Only the horizontal component of the laser is collimated, as it is not possible to collimate the laser both vertically and horizontally since it diverges at different rates along these axes.

### A.2.4 Grating alignment

The mirror mount is attached to an optics base plate. The grating is epoxied in a lower corner of the mirror mount in front of the adjustment screw as shown in Figure A.5. This adjustment screw allows horizontal alignment of the grating, while the other screw allows vertical grating alignment. The PZT is placed in the mirror mount between the horizontal adjustment screw and the front of the mount as shown in Figure A.5. The grating is then placed in front of the diode. It is angled such

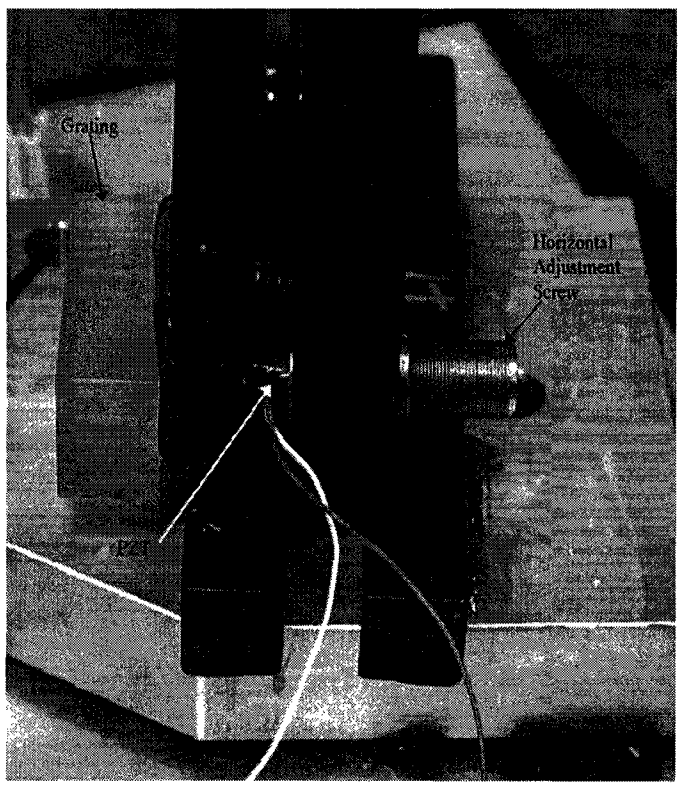



Figure A.5: This is a close-up picture showing the position of the PZT in the mirror mount on which the grating is mounted.

that the first order diffraction beam is sent back into the diode laser. The zeroth order is the laser output. Tuning of the laser is easier if the grating is as close as possible to the diode, yet far enough away that the output is not clipped by the lens

holder. The first diffraction order is verified to be reflected back into the diode and not hitting the lens housing by turning the lights off and looking to see if any light is noticeable on the lens housing. The IR viewer can be useful for this purpose, but we usually find it difficult to observe due to the amount of light being emitted from the laser. The grating is epoxied onto the flexure mount once it is satisfactorily placed and the two leads of the PZT are connected to the BNC connector.

In order for proper feedback, the grating must be aligned vertically as well. This process requires a lot of patience and it seems that everyone has his or her own technique for accomplishing this. I will describe my method and another method that has been useful but is not always possible. Using the uppermost adjustment screw (the vertical adjustment screw), the grating is misaligned greatly so that the first order is known to hit above the diode. While this may seem counterproductive, it determines which direction the grating will have to be moved in order to align it properly. The current is turned down until it is just below threshold, which is the current at which the laser begins to lase. The threshold current can be determined by measuring the output of the diode as a function of current using a power meter. When the data is plotted, a specific current at which a dramatic increase in the laser power is evident. Such a plot should be made for each laser, as one sign of failure is an increase in the threshold current. Such a graph is shown in figure A.6.

With the lights off and the power supply just below threshold, an allen wrench is used to slowly turn the vertical adjustment screw while the laser output is observed on an infrared detector card. When the grating is aligned, the intensity of the output will increase. If the power supply is tuned too far below or above threshold, this

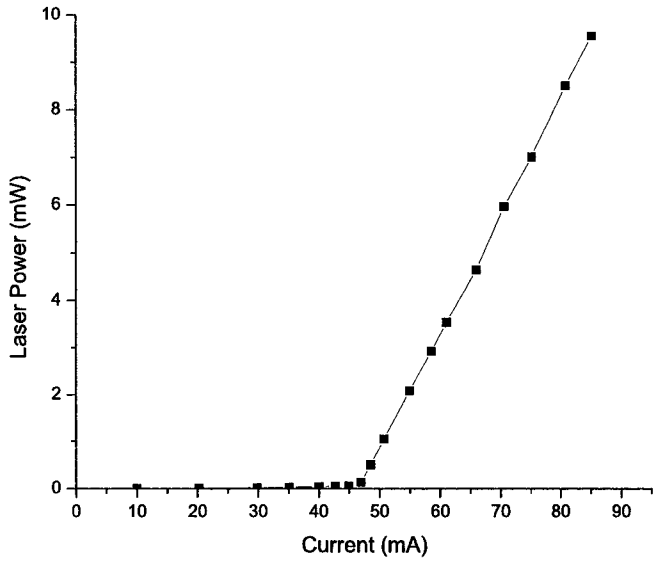



Figure A.6: A graph of the laser power as a function of the current supplied. The laser power increases slowly until the threshold current at 47 mA, after which the laser power increases much more rapidly.

increase in intensity may not be noticeable. When the grating is aligned as such, the threshold current is lowered a small amount. The power supply should again be turned down slightly below threshold and the grating alignment adjusted again as described above. This results in a more accurate alignment.

Another method we use for vertically aligning the laser is called the "two dot method". This method, however, does not always work. The laser is first directed onto the wall. With the current set well above threshold the night vision camera is used to observe the beam on the wall. There may be two dots–a very bright one from the laser and a second dimmer dot either above or below it. The second dot may also be slightly off to one side. Using the vertical adjustment screw, the two

dots are overlapped. The power supply is then turned down to the threshold current and the above method is used to verify and more accurately align the grating.

## A.3 Temperature Control

The frequency of the laser output depends upon both the grating position and the temperature. For stable laser operation the temperature is controlled using both a heater and a cooler. The aluminum lid is insulated with insulating foam. We use two different types of controllers manufactured by Wavelength Electronics: the RHM-4000 and the MPT-2500. The RHM-4000 controller has jumpers to switch between using it as a cooler and as a heater. It also has another jumper that determines the amount of current that will be sent through the thermistor which should be set at the 100 $\mu$A setting. The RHM-4000s are placed in the rack built for them and are powered by two power supplies at 20 V. Cables with male 4-pin connectors on each end are constructed to go between the RHM-4000's and the lasers. The voltage read from the temperature monitor (Tmon BNC output) of each RHM-4000 is converted to a resistance and compared with the chart provided with the thermistor in order to determine the temperature. The temperature set point is read in the same manner and is changed using the potentiometer screws on the front of the RHM-4000. Typically, to begin with, the cooler is set 2-3 °C below room temperature and the heater is set 2-3 °C above room temperature. It is normal for the temperature of the laser to stabilize at a temperature slightly above or below the set point. When the controller is first connected to the laser, most likely there will

be a large current draw (>1 A). After a few minutes the temperature of the laser should reach the set point and the current draw should decrease. If the current draw remains more than 1 A, most likely something is connected backwards: the cooler leads may be connected backwards so that the TEC is heating the laser rather than cooling it or the RHM-4000 may be set as a heater instead of a cooler or vice-versa. Another possibility is a faulty controller.

The MPT-2500 temperature controllers are designed to be used with a TEC only and operate differently than the RHM-4000 temperature controllers. With the RHM-4000, if the temperature of the cooler falls below the set point the current supplied to the TEC is turned off, and the same occurs if the temperature of the heater rises above the set point. With the MPT-2500, however, if the cooler temperature drops below the set point, the current direction is reversed. This does not work with the resistive heater films that we use in that they heat when current is passed through them regardless of the direction. We have solved this by placing a diode in the cable connecting the MPT-2500 with the heater that opposes the current in the direction from the $TEC^+$ to $TEC^-$ outputs of the controller.

## A.4 Tuning the laser

Tuning the laser is done using a combination of temperature, grating, and current adjustments. The frequency of the laser is determined by directing its output into a Burleigh wavemeter. If the laser is lasing in a single mode, the wavemeter will display the frequency as a stable number with $< 1$ GHz fluctuations, and the power

meter located on the side of the display will also be stable. Most likely, when the laser is directed into the wavemeter for the first time it will not be lasing in a single mode. Several different signs of this can be observed on the wavemeter: the frequency displayed may fluctuate rapidly, the display will not show a frequency but will alternate between "HI SIG" and "LO SIG", or the power will be shown as fluctuating rapidly. A combination of these symptoms is also possible. The laser should stabilize with a small adjustment in the current. If not, then the grating should be re-vertically aligned and the laser aligned into the wavemeter again.

Once the laser is operating in a single mode, it will most likely be within 1000 GHz from the desired operating frequency. The laser is tuned by adjusting the grating while observing the wavemeter. If the frequency of the laser needs to decrease, the grating is moved away from the laser (the horizontal adjustment screw is let out), whereas the grating is moved closer to the laser if the laser frequency needs to increase.

The laser may also cease lasing in a single mode as the grating is adjusted. Sometimes this may be corrected with an adjustment in the current; otherwise the grating may need to be re-vertically aligned. The laser needs to be vertically aligned periodically while it is being tuned. As the laser is being tuned, there also may be a point where its frequency jumps a large amount. This is a mode hop, and small temperature adjustments can shift the position of the mode hop so that it is possible to tune the laser to the desired frequency.

## A.5 Master Oscillator Power Amplifier

A power amplifier is a device that amplifies up to 5 mW of power from the diode laser (master oscillator) to 500 mW at the same frequency. These devices are very expensive and static sensitive. The amplifiers that we possess have already had the power connections soldered. The temperature control is much simpler as they only need to be cooled and not heated. The alignment of the diode laser into the amplifier is critical for efficient amplification. The alignment process is described in this section. A picture of our MOPA setup is shown in Figure A.7.

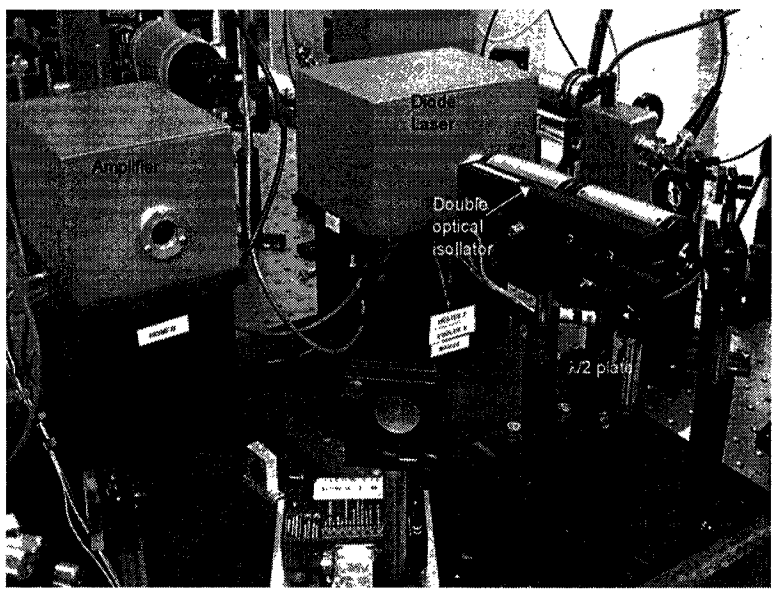



Figure A.7: This is a picture of the MOPA setup. The output of the diode laser passes through the double optical isolator and then through the $\lambda/2$ plate before entering the amplifier.

A power supply is connected to the amplifier and is typically set at 1.35 A. When power is supplied to the amplifier, fluorescence is emitted from both the front and the back of the device. The fluorescence emitted from the back is much weaker than

what is emitted from the front. It is the back fluorescence that enables alignment of the diode laser, and it must be collimated in the same manner described in section A.2.3. This collimation is critical in obtaining efficient amplification. A double optical isolator, which acts as a light diode to minimize on feedback from laser reflection and the back fluorescence of the amplifier, is placed in front of the diode laser. These devices have a polarizer on the input. A Faraday rotator then rotates the polarization by 45°. Reflections back into the isolator are rotated again by 45° in the same direction so that the polarization of any back reflections is perpendicular to the input polarizer. Generally, single optical isolators are sufficient, but we have noticed that some of the back fluorescence from the amplifier gets through a single optical isolator and interferes with the laser operation. A $\lambda/2$ plate is used to adjust the polarization of the laser after it exits the optical isolator. The amplifier requires a vertically polarized input. A polarizing beam splitter cube is used to separate the light into vertical and horizontally polarized components. The vertically polarized light is directed into the amplifier, while the horizontally polarized component is used to lock the laser as described in section B.3. The $\lambda/2$ plate is adjusted so that no more than 5 mW is in the vertically polarized component that enters the amplifier.

The vertically polarized component of the diode laser is directed into the amplifier using the collimated back fluorescence as a guide. Once there is amplification, the fluorescence from the front side of the amplifier has a bright horizontal line through it. A laser power meter is placed in front of the amplifier and the diode laser alignment is tweaked until the maximum power is obtained. It is essential that no

more than 500 mW power is emitted from the amplifier. If the power exceeds this level then the amplifier may become permanently damaged. The power emitted by the amplifier is proportional to the current supplied. If the output nears 500 mW, the current needs to be decreased so that the laser is at a safer level.

# Appendix B

# Locking the Laser to Atomic Transitions

## B.1 Introduction

Diode lasers are useful for laser cooling and trapping experiments in $^{87}$Rb because they have a narrow bandwidth, are inexpensive, and are mass-produced at frequencies near the $^{87}$Rb $^2S_{1/2} \rightarrow {}^2P_{3/2}$ transition frequencies; however, the frequency outputs of diode lasers are characteristically unstable, and are dependent upon temperature, grating alignment, and current. While an external cavity configuration reduces these instabilities, small temperature changes or mechanical vibrations can result in significant frequency drifts. For most laser cooling and trapping applications it is necessary for the laser to be stable near one of two atomic hyperfine transition frequencies: the cycling and the repump frequencies [22]. Thus, some method of locking the lasers to these atomic transition frequencies is required to obtain more stability in the trap.

We can electronically control the grating position, and thus the laser frequency, by changing the voltage applied to the piezoelectric transducer (PZT) located behind

the grating. Some sort of electronic feedback signal is necessary to determine if the laser is lasing at the desired frequency and, if not, in what direction the grating should be moved. Such a signal can be generated using a saturated absorption spectrometer [37, 38] or a dichroic atomic vapor laser lock (DAVLL) [39]. Once this signal is generated, an electronic feedback loop can be created to continuously change the grating position so that the laser remains at the desired frequency.

## B.2 Saturated Absorption Spectroscopy

Saturated absorption spectroscopy is a Doppler free method of obtaining the atomic transition frequencies. The resulting signal shows the resonances as small sharp peaks. The saturated absorption spectrometer setup is shown is Fig. B.1. A small

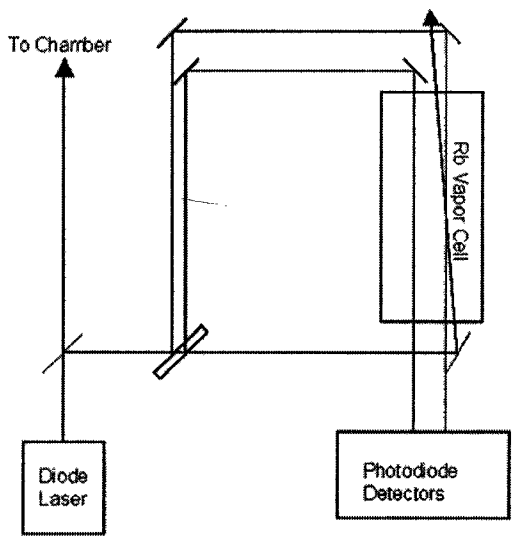



Figure B.1: Optical setup of the saturated absorption spectrometer

fraction of the diode laser output is picked off and sent to the spectrometer to use for locking. The remaining light is sent to the system to be used in the experiment.

The light to be used in the spectrometer is first sent through a non-coated glass window that is positioned at an angle relative to the incoming beam. Small portions of the beam are reflected from the front and back faces of the window. These two beams are directed through a Rb vapor cell and into photodiode detectors. The light transmitted through the windows is directed through the vapor cell in an opposing direction to the weak beams generated from the faces of the window. This more intense beam is aligned such that it nearly overlaps one of the weak beams (probe beam). When the intense beam passes through the Rb vapor, it pumps atoms into the excited state when these atoms are Doppler shifted into resonance with the laser. The weaker probe beam in the opposing direction will de-excite the atoms when they are Doppler shifted into resonance with it. Because these two beams are in opposing directions, the atoms will only be Doppler shifted into resonance with both lasers when their velocity is 0 and the laser is on resonance [38]. The Doppler broadened absorption profile of this probe beam then has a sharp peak when the laser is on resonance. The second weak beam is used to subtract the Doppler broadened absorption profile, leaving only the sharp peaks when the laser is on resonance with the atomic transitions.

A triangle wave is applied to the PZT controlling the laser grating which sweeps the laser frequency. The electronic signals from the two photodiode detectors are subtracted and the resulting signal shows sharp peaks at the resonant frequencies on a nearly flat background similar to that shown in Figure B.2. Sharper peaks are obtained by optimizing the alignment of the overlapping beams.

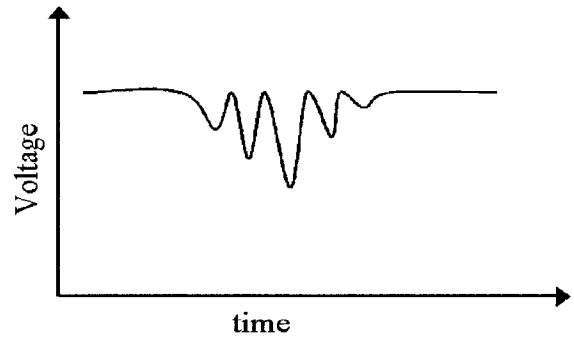



Figure B.2: This is an example of a saturated absorption spectroscopy signal observed on an oscilloscope.

## B.3 Dichroic Atomic Vapor Laser Lock (DAVLL)

The DAVLL is another method of obtaining an electronic signal to be used in the laser feedback loop. The curves obtained are very large and Doppler broadened. It is therefore only applicable to use the DAVLL independently if the absolute values of the atomic transition frequencies do not need to be determined. Locking the laser using the DAVLL signal is much easier than with the saturated absorption spectrometer because of the size of the curves. For applications in which we need to accurately determine the locations of the resonant frequencies we use the saturated absorption spectrometer to locate these, but we lock the laser using the DAVLL.

A schematic of the DAVLL is shown in Fig. B.3. As performed with the saturated

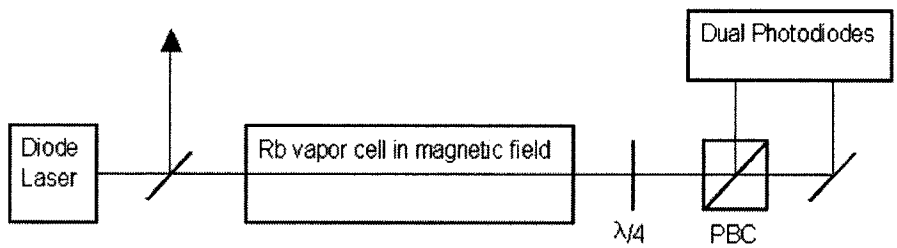



Figure B.3: Schematic of the DAVLL

absorption spectrometer, a small portion of the diode laser output is picked off to be used for the laser lock, while the remaining light is sent to the system to be used in the experiment. The beam used in the lock is directed through a Rb vapor cell that is placed in a uniform magnetic field. The ~100 G magnetic field, which serves to shift the atomic levels, is created by placing the Rb vapor cell in the centers of rings of permanent magnet material separated by plastic spacers.

The linearly polarized light from the diode laser is a superposition of equal components of left and right ($\sigma^-$ and $\sigma^+$) circularly polarized light. The selection rules for an atom to absorb $\sigma_\pm$ light is that $\Delta m = \pm 1$. When the Rb vapor is not placed in a magnetic field, the Doppler broadened absorption profiles overlap. The magnetic field serves to separate the Doppler broadened absorption profiles for the two circularly polarized components of light and shifts them in opposite directions. The two circularly polarized components are separated into orthogonal linear components by the $\lambda/4$ plate. The resulting beams are then directed into photodiode detectors and the electronic signals are subtracted. When the laser frequency is ramped by applying a triangle wave to the PZT located behind the laser grating the resulting signal looks similar to that shown in Figure B.4.

## B.4 Sidelock Servo Box

Once a signal has been generated by either a saturated absorption spectrometer or a DAVLL it can be used to lock the laser provided that signal is sloped at the desired frequency and is not a maximum or minimum. We use a home built sidelock servo

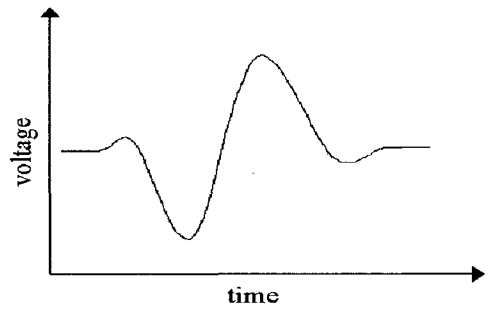



Figure B.4: This is an example of a DAVLL curve observed on an oscilloscope.

box to electronically determine when the laser is drifting off frequency and make grating adjustments accordingly.

The DAVLL signal is sent into the servo box. When the laser is locked the servo box reads the DAVLL signal and adjusts the grating so that the signal read is always 0 V. One can pick which point on the slope the laser is to be locked by adding a bias voltage to the DAVLL signal. The laser can be locked to either a positive or a negative slope by changing the PZT polarity. In this section, the locking process is described.

A diagram of the sidelock servo box is shown in figure B.5. For our purposes the

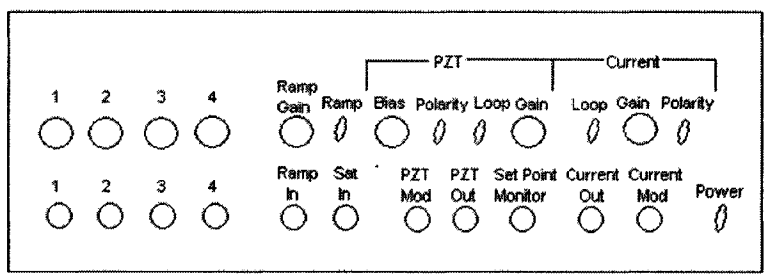



Figure B.5: Front panel schematic of the sidelock servo box used to lock the lasers to the atomic frequency.

current MOD and Current Out connections are not used. The triangle waveform from the function generator is connected to the Ramp In input. The laser frequency is ramped by connecting the PZT to the PZT Out connection of the servo box. The signal from the DAVLL or the saturated absorption spectrometer is connected to the SAT IN input and is observed by connecting an oscilloscope to Set Point Monitor. We ground the PZT Mod and Laser Unlock connectors using 50 $\Omega$ terminators.

The ramp gain knob adjusts the amplitude of the ramp applied to the PZT. When the knob is turned completely to the left, the amplitude applied to the PZT is the same as that of the function generator connected to Ramp In. The amplitude decreases as the knob is turned clockwise until it reaches the stopping point at which time the amplitude is zero. The Ramp switch controls whether a ramp is applied to the PZT regardless of the status of the Ramp Gain knob. When this switch is in the down position no ramp is applied to the PZT. The PZT Bias knob adds a bias voltage to the ramp applied to the PZT. When no ramp is applied, the Ramp Bias determines the voltage applied to the PZT.

The PZT switch determines whether or not the feedback loop used to lock the laser is activated. If the switch is in the up position, the feedback loop is not activated and the laser is not locked. If the switch is in the down position, the servo box reads the Sat In signal and tries to adjust the PZT so that the Set Point Monitor output is consistently 0 V. If it is desired that the laser not be locked, but rather ramped over the atomic transition so that the saturated absorption features can be observed, the ramp switch should be up, the PZT loop switch should be up, and the Ramp Gain knob should be turned to the far left.

The procedure to lock the laser to the atomic transition frequency begins with determining where on the saturation absorption signal or the DAVLL signal the laser needs to be locked. If the DAVLL or saturated absorption signal is a maximum or minimum at that point, it will not be possible to lock the laser. The DAVLL signal can be adjusted by turning the $\lambda/4$ plate or the derivative of the saturated absorption signal can be obtained by applying a dither to PZT Mod and using a lock in amplifier. The output of the amplifier is then connected to Sat In.

The point on the signal that the laser is to be locked at is dialed in using the Ramp Gain and the Ramp Bias knobs. While observing the Set Point Monitor on an oscilloscope, the Ramp Gain knob is turned to the right and the Ramp Bias knob is used to keep the area of the signal that the laser is to be locked to in the center of the oscilloscope's display. When the Ramp Gain knob is turned completely to the right, the Ramp Switch should be turned off.

The servo box tries to keep the Set Point Monitor output at 0 V when the feedback loop is activated. When the area at which the laser is to be locked to is dialed in, the Set Point Monitor is generally not at 0 V. The knobs labeled 1-4 are used to add a bias voltage to the Set Point Monitor output, which can raise or lower the signal displayed on the oscilloscope. The knob is selected by grounding the corresponding BNC connector located below it with a 50 $\Omega$ terminator. The remaining 3 connectors should be set to 5 V which disables those corresponding knobs. Once the Set Point Monitor signal displayed on the oscilloscope is at 0 V the laser can be locked by switching the PZT loop switch to the down position. If the signal on the oscilloscope starts to move away from 0 V when the laser is first locked,

the PZT polarity switch is most likely in the wrong position. Another possibility is that the laser is being locked at a position where there is no slope on the saturated absorption or DAVLL signal. Once locked, the frequency of the laser can be changed slightly by adjusting the numbered knob selected with the 50 $\Omega$ terminator.

# Appendix C

# Vacuum

The number of atoms in a MOT is limited by collisions from the background gas [22]. Vacuum pressures of less than $10^{-10}$ Torr are desirable to reduce these collisions. Cleanliness is of great importance in achieving such vacuum pressures as any contaminant in the system will outgas and limit the achievable vacuum to the vapor pressure of the contaminant. We only achieved pressures these low for a short period of time. The majority of our experiments were performed at vacuum pressures near $10^{-7}$ Torr.

## C.1 Vacuum pumps

Among the many different types of vacuum pumps available are diffusion pumps, turbo pumps, and ion pumps. Diffusion pumps have very large pumping speeds, but they are oil pumps and are very dirty. Thus diffusion pumps are not recommended for ultra-high vacuum. Turbo pumps are clean, have pumping speeds up to 300 L/s, and can achieve vacuum pressures of less than $10^{-10}$ Torr. However, they are mechanical

pumps and thus add mechanical vibrations to the system. Ion pumps can be made very clean and do not vibrate as they are non-mechanical, but they use very strong magnets and do not work well in experiments where stray magnetic fields are a problem. They also must be removed from the system and serviced periodically to have their elements changed. For our current experimental setup we are using only a turbo pump.

All of the vacuum pumps listed above can only be operated at pressures below $10^{-3}$ Torr. A separate vacuum pump must be used to rough the system to a lower pressure before the pumps listed above are operational. The turbo pump works like a very high-speed fan that rotates up to 56,000 RPM. It holds a pressure differential between the vacuum system and the roughing pump. It must have the roughing pump on continuously and the ultimate pressure is limited by how well it is roughed. The ion pump may be used alone once it has been roughed to the appropriate pressure and the roughing pump may be disconnected from the system. There are no mechanical parts used in the ion pumps, and thus all mechanical vibrations from the vacuum system may be eliminated in this manner.

The selection of a roughing pump also is important. Diaphragm pumps are oil free and eliminate the worry of contamination from pump oil flowing back into the system. Mechanical pumps contain oil, but they offer a lower roughing pressure than that achievable with diaphragm pumps. This lower roughing pressure allows the turbo pump to ultimately achieve a lower vacuum pressure. A filter can be installed to help prevent oil from contaminating the system, however it will not necessarily eliminate it. An electronic valve should also be installed between the

roughing pump and the vacuum system that will close in the event of a power failure. This will help to maintain a lower pressure in the system and will eliminate oil from flowing between the pump and the system when the power is off. We currently are using a mechanical pump with an oil filter in conjunction with our turbo pump to achieve lower vacuum pressures.

## C.2 Cleaning

Any contaminants within the system, even something as small as a fingerprint, will outgas and destroy the vacuum. Cleaning should be done meticulously so as to remove all contaminants and avoid introducing others. Powder free latex gloves should be worn at all stages of the cleaning and assembly processes. These gloves should be changed often. It is also necessary to avoid touching any interior surface of the vacuum system with even a gloved hand. Oil-free aluminum foil should cover all areas of the workstation. Aluminum foil purchased from the grocery store is manufactured for cooking purposes and contains oil to reduce sticking. We have purchased high-vacuum aluminum foil from All Foils, Inc. for vacuum purposes. It should be noted that you can only get your parts as clean as the tools used in the cleaning process. In other words, make sure that anything used in the cleaning process is as clean as possible.

The first step in the cleaning process is degreasing. We use the large sonicator in the shop with degreasing detergent for this purpose. Any water left in the sonicator from previous used must be drained, and the sonicator must be cleaned with the

degreasing solution before any parts are cleaned. The tub is then be filled with the appropriate amount of detergent added. Once the tub is filled and the water is heated the sonicator can be turned on. It is very loud and ear protection is recommended. The parts that are being cleaned are suspended in the solution as close to the center of the tub as possible using bare copper wire. To insure proper cleaning the parts should not touch the sides or bottom of the tub if at all possible. After each part has been sonicated for approximately 5 minutes it is removed from the solution and placed on oil-free aluminum foil.

The part is then rinsed well using deionized water. Care is taken that the parts do not come into contact with the water container, and that the interior surfaces are not touched by even gloved hands. The part is then rinsed with Ultima quality acetone to remove the water. The acetone is removed with Ultima quality methanol. The part is wrapped with the oil-free aluminum foil until it is ready to be assembled after the methanol has been allowed to evaporate.

## C.3 Assembly

We use copper gaskets and silver plated bolts in assembling the vacuum system. Viton gaskets are reusable and easier to use, but these gaskets are not bakeable. We use silver plated bolts for easier removal when disassembling the system after baking.

Before assembly the knife-edge of each part is inspected for any imperfections or debris that could prevent a good seal from forming and limit the vacuum pressure.

The knife-edge is then cleaned using a clean-room grade wipe with Ultima grade methanol to remove anything that may have been missed in the cleaning process. As cleanliness is of utmost importance, each wipe is only used once and is not swiped multiple times over the surface. The copper gasket is cleaned in the same manner and placed in the groove located on a part. The joining part is connected and the bolts with washers are directed through the bolt holes and screwed into platenuts. Before wrench tightening is done, the bolts are all finger tightened. The bolts are tightened in a star pattern to ensure that the gasket is sealed evenly. It is necessary to take care that the bolts are all tightened the same amount each iteration. The bolts should continue to be tightened until no copper can be seen between the two joining surfaces.

## C.4 Pumping Down

After the system has been completely assembled, one last inspection is performed to make sure that all of the seals appear to be good. The roughing pump is first turned on, and the pressure is monitored using a thermocouple gauge. The turbo pump is started after the pressure falls below $10^{-3}$ Torr and the roughing pump is no longer making a lot of noise. It may take up to 8 minutes before the turbo pump is operating at full speed after which the ion gauge can be turned on to monitor the pressure.

Data is taken to monitor the rate at which the system pumps down. If the ion pump is going to be used it is turned on after the pressure has fallen well below $10^{-5}$

Torr. A pressure spike is generally observed after the ion pump has been turned on. Data is also taken to record the time it takes for the pressure to spike, how high the pressure spikes to, and the rate at which it decreases. After the pressure levels off and no longer decreases, the ion gauge is degassed in order to get a more accurate pressure reading. Once again the pressure usually spikes and data is taken. The degas should be turned off after about 10 minutes or so and the pressure should continue to be recorded until it has leveled out.

After the pressure levels off, the system is checked for leaks by spraying methanol around the seals and any welds. A leak is observed as a sudden increase or decrease in the pressure after the methanol is sprayed on an area. A leak at one of the seals may be fixed by tightening the bolts. Leaks in welds require the system to be brought back up and those portions disassembled and re-welded either by our shop or at the manufacturers.

## C.5 Baking

To achieve the best pressure possible, the system is baked at a high temperature for a long period of time. When the system is heated, any contaminants within the system will outgas quickly and be pumped away. Before baking, an understanding of the maximum temperatures that the various components can be reached is necessary. Components, such as the turbo pump, that cannot exceed 100° C should be left outside of the baking region and not directly heated. Ion pumps cannot be baked more than 200° C because of the magnets. If the magnets are removed before baking

the temperature can be increased. Thermistors are placed at strategic areas of the system to monitor the temperature. We have used two different methods to bake the chamber, both of which have their advantages and disadvantages.

The first method we have used involves wrapping the chamber with heating tape and then wrapping that with fiberglass insulation. The disadvantage to this method is that it does not allow for even heating, and hot spots occur where the chamber is in direct contact with the heating tape. It is, however, easy to set up and is relatively clean compared with the other method we have used. This other method involves creating a brick oven on the table around the chamber with 2 oven elements resting at the bottom. This method is messy, but provides a much more even baking.

After the heat source is turned on, data is taken to monitor the source setting, the pressure, and the temperature. The pressure will increase as the system is heated, and there may be instances when the pressure increases more rapidly than others. After some time at the desired temperature, the system pressure will level off and then begin to decrease. The heat source should be turned off after it has been determined that the pressure is no longer decreasing–generally this will be a number of days after the baking process has been started. As the system cools, the pressure will decrease rapidly and data should continue to be taken. After the system cools completely, the pressure is hopefully lower than it was before the baking process was started. If not then there is a leak or some other catastrophic problem.

# Bibliography


[1] Steven Chu. The manipulation of neutral particles. *Rev. Mod. Phys.*, 70(3):685–706, July 1998.

[2] William D. Phillips. Laser cooling and trapping of neutral atoms. *Rev. Mod. Phys.*, 70(3):721–741, July 1998.

[3] Claude N. Cohen-Tannoudji. Manipulating atoms with photons. *Rev. Mod. Phys.*, 70(3):707–720, July 1998.

[4] E. A. Cornell and C. E. Wieman. Nobel lecture: Bose-Einstein condensation in a dilute gas, the first 70 years and some recent experiments. *Rev. Mod. Phys.*, 74(3):875–893, July 2002.

[5] Wolfgang Ketterle. Noble lecture: When atoms behave as waves: Bose-Einstein condensation and the atom laser. *Rev. Mod. Phys.*, 74(4):1131–1151, October 2002.

[6] S. J. M. Kuppens, K. L. Corwin, K. W. Miller, T. E. Chupp, and C. E. Wieman. Loading and optical dipole trap. *Phys. Rev. A*, 62:013406, 2000.

[7] J. D. Miller, R. A. Cline, and D. J. Heinzen. Far-off-resonance optical trapping of atoms. *Phys. Rev. A*, 47(6):R4567–R4570, June 1993.

[8] Nir Friedman, Ariel Kaplan, and Nir Davidson. Dark optical traps for cold atoms. *Adv. Atom. Mol. Opt. Phys.*, 48:99–151, 2002.

[9] Anthony E. Siegman. *Lasers.* University Science Books, 1986.

[10] J. Arlt, K. Dholakia, L. Allen, and M. J. Padgett. The production of multiringed laguerre-gaussian modes by computer-generated holograms. *J. Mod. Optic.*, 45(6):1231, 1998.

[11] Sharon A. Kennedy, Matthew J. Szabo, Hilary Teslow, James Z. Porterfield, and E. R. I. Abraham. Creation of Laguerre-Gaussian laser modes using diffractive optics. *Phys. Rev. A*, 66:043801, 2002.

[12] Eric R. I. Abraham and Michael A. Morrison. Prospects for an atomic clock in a laser trap. *B. Am. Phys. Soc.*, 47:36, 2002.

[13] Norman Ramsey. *Molecular Beams.* Oxford University Press, 1956.

[14] Mark A. Kasevich, Erling Riis, Steven Chu, and Ralph G. DeVoe. rf spectroscopy in an atomic fountain. *Phys. Rev. Lett.*, 63(6):612–615, August 1989.

[15] S. Chu and K. Gibble. Laser-cooled Cs frequency standard and a measurement of the frequency shift due to ultracold collisions. *Phys. Rev. Lett.*, 70(12):1771–1774, March 1993.

[16] S. Ghezali, Ph. Laurent, S. N. Lea, and A. Clairon. An experimental study of the spin-exchange frequency shift in a laser-cooled cesium fountain frequency standard. *Europhys. Lett*, 36(1):25–30, 1996.

[17] J. Tempere, J. T. Devreese, and E. R. I. Abraham. Vortices in Bose-Einstein condensates confined in a multiply connected Laguerre-Gaussian optical trap. *Phys. Rev. A*, 64(2):023603, August 2001.

[18] B. P. Anderson, K. Dholakia, and E. M. Wright. Atomic-phase interference devices based on ring-shaped Bose-Einstein condensates: Two-ring case. *Phys. Rev. A*, 67:033601, 2003.

[19] M. H. Anderson, J. R. Ensher, M. R. Matthews, C. E. Wieman, and E. A. Cornell. Observation of Bose-Einstein condensation in a dilute atomic vapor. *Science*, 269:198–201, July 1995.

[20] C. C. Bradley, C. A. Sackett, J. J. Tollett, and R. G. Hulet. Evidence of Bose-Einstein condensation in an atomic gas with attractive interactions. *Phys. Rev. Lett.*, 75(9):1687–1690, 1995.

[21] K. B. Davis, M.-O. Mewes, M. R. Andrews, N. J. van Druten, D. S. Durfee, D. M. Kurn, and W. Ketterle. Bose-Einstein condensation in a gas of sodium atoms. *Phys. Rev. Lett*, 75(22):3969–3972, 1995.

[22] Harold J. Metcalf and Peter van der Straten. *Laser Cooling and Trapping.* Springer-Verlag, 1999.

[23] Daniel A. Steck. Rubidium 87 D line data. *http://george.ph.utexas.edu/~dsteck/alkalidata/rubidium87numbers.pdf.*

[24] M. Harris, C. A. Hill, and J. M. Vaughan. Optical helices and spiral interference fringes. *Opt. Commun.*, 106:161–166, 1994.

[25] L. Allen, M. W. Beijersbergen, R. J. C. Spreeuw, and J. P. Woerdman. Orbital angular momentum of light and the transformation of laguerre-gaussian laser modes. *Phys. Rev. A*, 45(11):8185–8189, June 1992.

[26] E. Abramochkin and V. Volostnikov. Beam transformations and nontransformed beams. *Opt. Commun.*, 83(1,2):123–135, May 1991.

[27] M. W. Beijersbergen, R. P. C. Coerwinkel, M. Kristensen, and J. P. Woerdman. Helical-wavefront laser beams produced with a spiral phaseplate. *Opt. Commun.*, 112:321–327, December 1994.

[28] G. A. Turnbull, D. A. Robertson, G. M. Smith, L. Allen, and M. J. Padgett. The generation of free-space laguerre-gaussian modes at millimeter-wave frequencies by use of a spiral phaseplate. *Opt. Commun.*, 127:183–188, June 1996.

[29] N. R. Heckenberg, R. McDuff, C. P. Smith, and A. G. White. Generation of optical phase singularities by computer-generated holograms. *Opt. Lett.*, 17(3):221–223, February 1992.

[30] M. A. Clifford, J. Arlt, J. Courtial, and K. Dholakia. High-order laguerre-gaussian laser modes for studies of cold atoms. *Opt. Commun.*, 156:300–306, November 1998.

[31] Philip R. Bevington and D. Keith Robinson. *Data Reduction and Error Analysis for the Physical Sciences.* McGraw-Hill, 1992.

[32] J. P. Gordon and A. Ashkin. Motion of atoms in a radiation trap. *Phys. Rev. A*, 21(5):1606–1617, May 1980.

[33] Kerson Huang. *Statistical Mechanics.* John Wiley & Sons, 1987.

[34] Vanderlei Bagnato, David E. Pritchard, and Daniel Kleppner. Bose-Einstein condensation in an external potential. *Phys. Rev. A*, 35(10):4354–4358, May 1987.

[35] Franco Dalfovo, Stefano Giorgini, Lev P. Pitaevskii, and Sandro Stringari. Theory of Bose-Einstein condensation in trapped gases. *Rev. Mod. Phys.*, 71(3):463–512, April 1999.

[36] I. S. Gradshteyn and I.M. Ryzhik. *Table of Integrals, Series, & Products.* Academic Press Inc., 1980.

[37] K. B. MacAdam, A. Steinbach, and C. Wieman. A narrow-band tunable diode laser system with grating feedback, and a saturated absorption spectrometer for cs and rb. *Am. J. Phys*, 60(12):1098–1111, December 1992.

[38] W. Demtröder. *Laser Spectroscopy: Basic Concepts and Instrumentation.* Springer-Verlag, third edition, 2003.

[39] Kristan L. Corwin, Zheng-Tian Lu, Carter F. Hand, Ryan J. Epstein, and Carl E. Wieman. Frequency -stabilized diode laser with the Zeeman shift in an atomic vapor. *App. Opt.*, 37(15):3295–3298, May 1998.